Geochemistry Geophysics Geosystems G3
AN ELECTRONIC JOURNAL OF THE EARTH SCIENCES
Published by AGU and the Geochemical Society

Article
Volume 5, Number 11
6 November 2004
Q11007, doi:10.1029/2004GC000728
ISSN: 1525-2027

Strain localization on an oceanic detachment fault system, Atlantis Massif, 30°N, Mid-Atlantic Ridge

Timothy Schroeder
Department of Environmental Earth Sciences, Eastern Connecticut State University, 83 Windham Street, Willimantic, Connecticut 06226, USA (schroedert@easternct.edu)

Barbara E. John
Department of Geology and Geophysics, University of Wyoming, P.O. Box 3006, Laramie, Wyoming 82071, USA

[1] Microstructural observations, mineral chemistry, and the spatial distribution of deformation fabrics recorded in outcrop samples collected from Atlantis Massif, the active inside corner high at 30°N, Mid-Atlantic Ridge, suggest that strain is localized near the subhorizontal domal surface hypothesized to be an exposed detachment fault. Deformation textures in peridotite and gabbro indicate that high-temperature (>500°C) strain occurred via crystal-plastic flow and diffusive mass transfer. Low-temperature (<400°C) shear zones containing brittle and semibrittle microboudinage textures in which tremolite, chlorite, and/or talc replace fractured serpentine or hornblende cut earlier formed high-temperature deformation fabrics in peridotite. Textures indicate strain was localized by cataclasis and reaction softening into zones of intense greenschist and subgreenschist grade metamorphism. Gabbro is only weakly deformed below amphibolite facies (<500°C), indicating that strain was partitioned into altered peridotite at low temperature. There is a clear relationship between deformation intensity and structural depth beneath the subhorizontal surface of the Massif. Discontinuous high-intensity crystal-plastic deformation fabrics are found at all structural depths (0–520 m) beneath the surface, indicating that high-temperature, granulite- and amphibolite-grade deformation was not localized in a single shear zone. In contrast, semibrittle and brittle low-temperature shear zones are concentrated less than 90 m structurally beneath the surface, and the most intensely brittlely deformed samples concentrated in the upper 10 m. Localization of brittle deformation fabrics near the upper surface of the massif supports the hypothesis that it is the exposed footwall of a detachment fault. The structural evolution of Atlantis Massif is therefore analogous to a continental metamorphic core complex. Strain was localized onto the fault by reaction-softening and fluid-assisted fracturing during greenschist- and subgreenschist-grade hydrothermal alteration of olivine, clinopyroxene, serpentine, and hornblende to tremolite, chlorite, and/or talc.

Components: 13,304 words, 15 figures, 5 tables.

Keywords: detachment fault; low-angle normal fault; megamullion; metamorphic core complex; oceanic core complex; slow-spreading ridges.

Index Terms: 3035 Marine Geology and Geophysics: Midocean ridge processes; 3040 Marine Geology and Geophysics: Plate tectonics (8150, 8155, 8157, 8158); 3660 Mineralogy and Petrology: Metamorphic petrology.

Received 18 March 2004; **Revised** 2 July 2004; **Accepted** 28 July 2004; **Published** 6 November 2004.

Schroeder, T., and B. E. John (2004), Strain localization on an oceanic detachment fault system, Atlantis Massif, 30°N, Mid-Atlantic Ridge, *Geochem. Geophys. Geosyst.*, *5*, Q11007, doi:10.1029/2004GC000728.

1. Introduction

[2] Lithospheric extension at slow-spreading mid-ocean ridges has been hypothesized to occur by low-angle normal faulting that forms structural features analogous to continental metamorphic core complexes. This hypothesis is based upon bathymetric and geophysical observations of domal

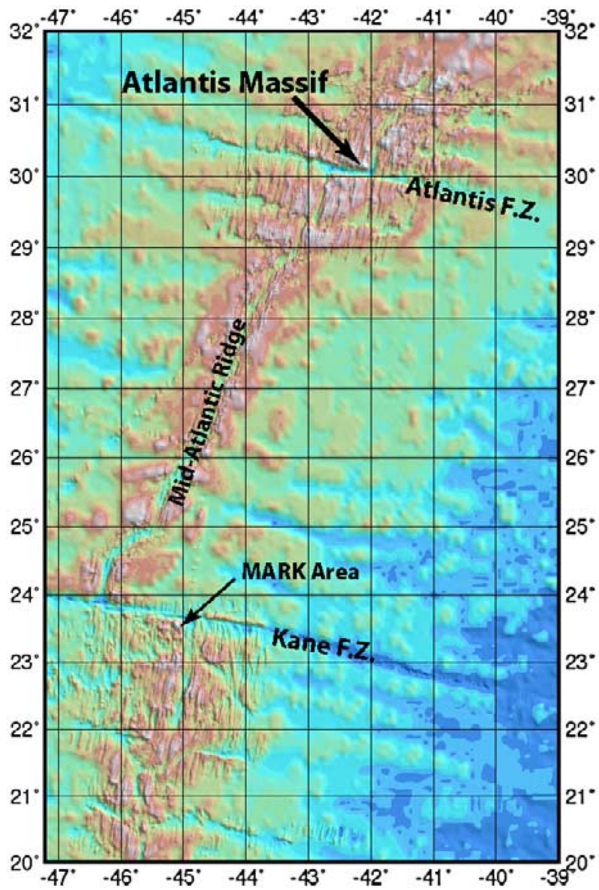

Figure 1. Map of the Mid-Atlantic Ridge from 20°N to 32°N showing the location of Atlantis Massif and the MARK area. Image modified from the Ridge Multibeam Synthesis Web site: http://ocean-ridge.ldeo.columbia.edu/.

culminations located at the inside corners of slow-spreading ridges (inside corner highs), and these features have been termed "oceanic core complexes" [*Tucholke et al.*, 1998; *Cann et al.*, 1997; *Blackman et al.*, 1998]. Geological sampling from two inside corner high sites along the Mid-Atlantic Ridge [*Dick et al.*, 1981; *Mutter and Karson*, 1992; *MacLeod et al.*, 2002; *Escartín et al.*, 2003] and one site on the Southwest Indian Ridge [*Dick et al.*, 1991; *Cannat*, 1991] also supports the oceanic core complex hypothesis. This study tests this hypothesis at an additional site with a detailed microtextural and mineral chemistry study of Atlantis Massif, an inside corner high located at the intersection of the Mid-Atlantic Ridge with the Atlantis Fracture Zone (30°N, Mid-Atlantic Ridge) (Figure 1), and attempts to determine the conditions and crustal level at which oceanic detachment faults are active. This site is the target of upcoming IODP Legs 304 (Core I) and 305 (Core II) that will attempt continuous drilling and sampling of an oceanic detachment fault system (http://www.usssp-iodp.org/Science_Support/sailing_information/occ_1_2.html).

[3] A metamorphic core complex is a domal culmination of mid- to lower-crustal rock surrounded by a low-angle normal (detachment) fault that separates structurally deep footwall rocks from hanging wall rocks of significantly higher structural level [*Crittenden et al.*, 1980; *Wernicke*, 1981]. Core complexes form in response to extreme tectonic extension by slip on normal faults that appear to dip approximately 5°–30° and penetrate to the middle or lower crust [*Crittenden et al.*, 1980; *Wernicke*, 1981; *John*, 1987; *Spencer and Reynolds*, 1989]. Core complexes were first recognized and defined in highly extended regions of the Basin and Range province of the North American Cordillera [*Crittenden et al.*, 1980; *Spencer and Reynolds*, 1989], and have subsequently been recognized in regions of highly extended continental lithosphere across the globe including the Anatolian region of Turkey [*Fayon et al.*, 2001; *Gessner et al.*, 2001], Greece and the Gulf of Corinth [*Chery*, 2001; *Bestmann et al.*, 2000], central China [*Zhang et al.*, 2000], and the Woodlark Basin off eastern Papua New Guinea [*Floyd et al.*, 2001]. The characteristic morphology of metamorphic core complexes is recognizable in nearly all occurrences, and includes a broad, elliptical dome of middle- to lower-crustal rock with long dimension between ∼10 km to 25 km (the footwall of the low-angle fault system). The dome is surrounded by rotated, block faulted ridges of upper-crustal rock that form the hanging wall [*Crittenden et al.*, 1980; *Davis et al.*, 1980]. In continental settings, the domed footwall is elevated up to 1000 m above the surrounding hanging wall, and is characterized by smooth, extension-parallel corrugations with wavelengths ranging from several hundred meters to tens of kilometers and amplitude ranging from tens to hundreds of meters [*John*, 1987].

[4] The oceanic core complex hypothesis suggests that the upper surface of an inside corner high is an exposed low-angle normal (detachment) fault that dips gently beneath the ridge axis upon which up to 5–10 km kilometers of extensional deformation is accommodated [*Dick et al.*, 1981; *Cann et al.*, 1997; *Tucholke et al.*, 1998; *Ranero and Reston*, 1999]. Inside corner highs have similar morphologic and geologic characteristics to continental metamorphic core complexes [*Tucholke et*

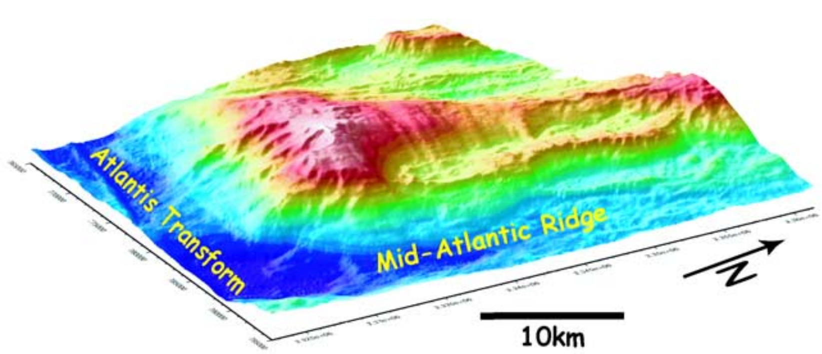

Figure 2. Three-dimensional bathymetric (oblique view) map of Atlantis Massif inside corner high. The morphology of Atlantis Massif and other inside corner highs strongly resembles a continental metamorphic core complex. Samples used for this study were dominantly collected from walls of landslide scarps along the southern margin (transform fault wall) of the massif.

al., 1997, 1998, 2001; *Cann et al.*, 1997; *Christie et al.*, 1997; *Mitchell et al.*, 1998; *Tamaki and Mevel*, 1998; *Escartín and Cannat*, 1999; *Searle et al.*, 1999]. The domal upper surfaces of inside corner highs have roughly the same degree of curvature as continental metamorphic core complexes. The undulating, spreading-parallel corrugations of the surfaces are of similar wavelength and amplitude to those observed on continental metamorphic core complexes (Figure 2) [*Blackman et al.*, 1998]. Angular ridges comprising pillow basalt are located between inside corner highs and adjacent axial valleys, and resemble the hanging wall of continental metamorphic core complexes [*Tucholke et al.*, 1998; *Blackman et al.*, 2004].

[5] In this paper we test the geological viability of oceanic core complex hypothesis by examining the evolution and spatial relations of deformation textures in rocks exposed at an active inside corner high, and compare them to those of a continental metamorphic core complex [*Crittenden et al.*, 1980; *Davis et al.*, 1980, 1986; *John*, 1987; *Spencer and Reynolds*, 1989] (Figure 3). These features in continental settings are formed as the footwall is denuded from high-temperature/high-pressure conditions in the middle to lower crust to surface temperature and pressure and include the following: (1) penetrative, gently dipping ductile deformation fabrics at structural levels up to 1000 m beneath the main detachment surface, (2) localized, ductile deformation fabrics with subhorizontal mylonitic foliation and extension-parallel lineations that crosscut penetrative fabrics within a mylonitic front up to several hundred meters beneath the detachment, (3) brittle, cataclastic deformation fabrics associated with intense low-temperature alteration that overprint all ductile fabrics and are localized into a zone between several meters and several hundred meters thick beneath the detachment fault; fabrics are dominantly subhorizontal, parallel to the inferred fault(s) and subparallel to oblique to mylonitic fabrics, and

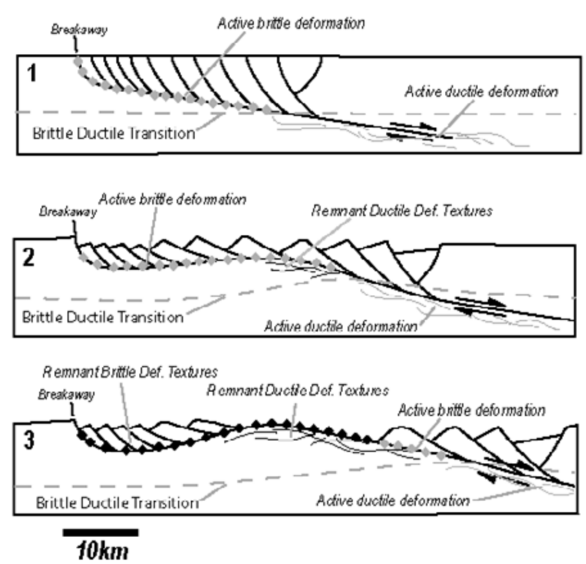

Figure 3. Idealized schematic cross sections depicting the development of a metamorphic core complex. In stage "1" the brittle fault and ductile shear zones are initiated with listric geometry. In stage "2," fault slip has resulted in rotation of hanging wall block toward the breakaway scarp, and the footwall begins to upwell as it is unloaded. In stage "3," footwall has been tectonically denuded and forms the metamorphic core complex dome, thereby exposing remnant mylonitic foliation formed below the brittle-ductile transition. (Modified from *Spencer* [1984]).

(4) a narrow (0–10 m) zone of unfoliated gouge that defines the main detachment.

2. Study Location

[6] Atlantis Massif is a domal uplift located at 30°N on the Mid-Atlantic Ridge (Figure 1). It is approximately 20 km long (parallel to the ridge axis) by 15 km wide. It stands 2000 m above the surrounding ridge flank and over 4000 m above the median valley floor. The site was first studied in detail during a R/V *Charles Darwin* cruise in 1996 that collected dredge samples and TOBI side-scan sonar data [*Cann et al.*, 1997; *Blackman et al.*, 1998, 2004]. Linear, spreading-parallel corrugations were recognized in the swath bathymetry as the upper surface of the massif [*Cann et al.*, 1997]. Samples were collected in 10 dredges from the central dome and surrounding ridges. These comprise serpentinized peridotite, gabbro and variable amounts of basalt from the central dome, suggesting complex geologic construction; samples from surrounding ridges were overwhelmingly basalt [*Cann et al.*, 1997; *Blackman et al.*, 1998]. Sea-surface gravity measurements indicate a gravity high beneath the central dome, which is suggested by *Blackman et al.* [1998] to represent mantle exposed at the seafloor. On the basis of these data, *Cann et al.* [1997] and *Blackman et al.* [1998] concluded that Atlantis Massif formed by tectonic denudation along a normal fault that dips gently beneath the Mid-Atlantic Ridge axis. Atlantis Massif was revisited in the Fall of 2000 by the MARVEL 2000 cruise of the R/V *Atlantis* (AT-03-60) to collect additional data with which to test the detachment fault hypothesis using methods described below.

3. Methods

3.1. Sample Collection and Seafloor Observation During MARVEL 2000 Cruise

[7] Outcrop and float samples were collected in 15 dives of the manned submersible *Alvin* (dive tracks shown in Figure 4), and poorly located (±500 m) samples were collected in two successful dredge hauls (Figure 4) [*Blackman et al.*, 2004]. *Alvin* sample locations are determined by sonar transponder navigation. Some samples are poorly to moderately well oriented by gyroscopic compass or visual techniques using video observation and concurrent submarine heading. The majority of the gently domed surface of Atlantis Massif is covered by a thin (<1 m), poorly to well-indurated carbonate deposit [*Kelley et al.*, 2001; *Schroeder et al.*, 2002; *Blackman et al.*, 2004] that prevented effective outcrop sampling of basement rocks. Most outcrop sampling was therefore accomplished on the headwalls of landslide scarps along the southern flank of the massif (Figure 4). A total of 137 samples ranging in size from 5 cm to 80 cm in diameter were collected with *Alvin*, 73 of which are used in this study (Table 1). Most samples are composed completely of gabbro or peridotite, with less abundant samples comprising peridotite with 0.5 cm to 2 cm wide gabbro dikes or veins. Gabbro and peridotite outcrops were found to be interspersed on scales ranging from 5 m to 100 m on steeply dipping slopes traversed on submersible transects. A complete discussion of sampling methods and rock distribution is given by *Blackman et al.* [2004].

3.2. Sample Analysis

[8] Igneous and metamorphic petrography, deformation textures, and veins in *Alvin* and dredge samples were described in hand sample during the MARVEL 2000 cruise. Thin sections were cut from selected samples on planes perpendicular to foliation and parallel to lineation directions when possible. Thin sections were studied with transmitted and reflected light optical microscopes to observe deformation textures and syn-deformation mineral assemblages. Selected samples were also analyzed with a scanning electron microscope to observe very fine-grained (<50 μm) deformation textures and to identify fine-grained alteration minerals. Amphibole and chlorite chemistry in metaperidotite samples, and amphibole and plagioclase in gabbro samples were analyzed to estimate the temperature of deformation (procedures detailed in Appendix A).

4. Strain History and Strain Fabric Description

[9] Deformation texture descriptions are presented in the order of their formation based on overprinting relations in an effort to establish the progression of deformation events. Deformation textures are divided into three broad categories: ductile, semibrittle, and brittle. Also described below are fabrics formed during serpentinization and static metasomatic alteration. No basalt sam-

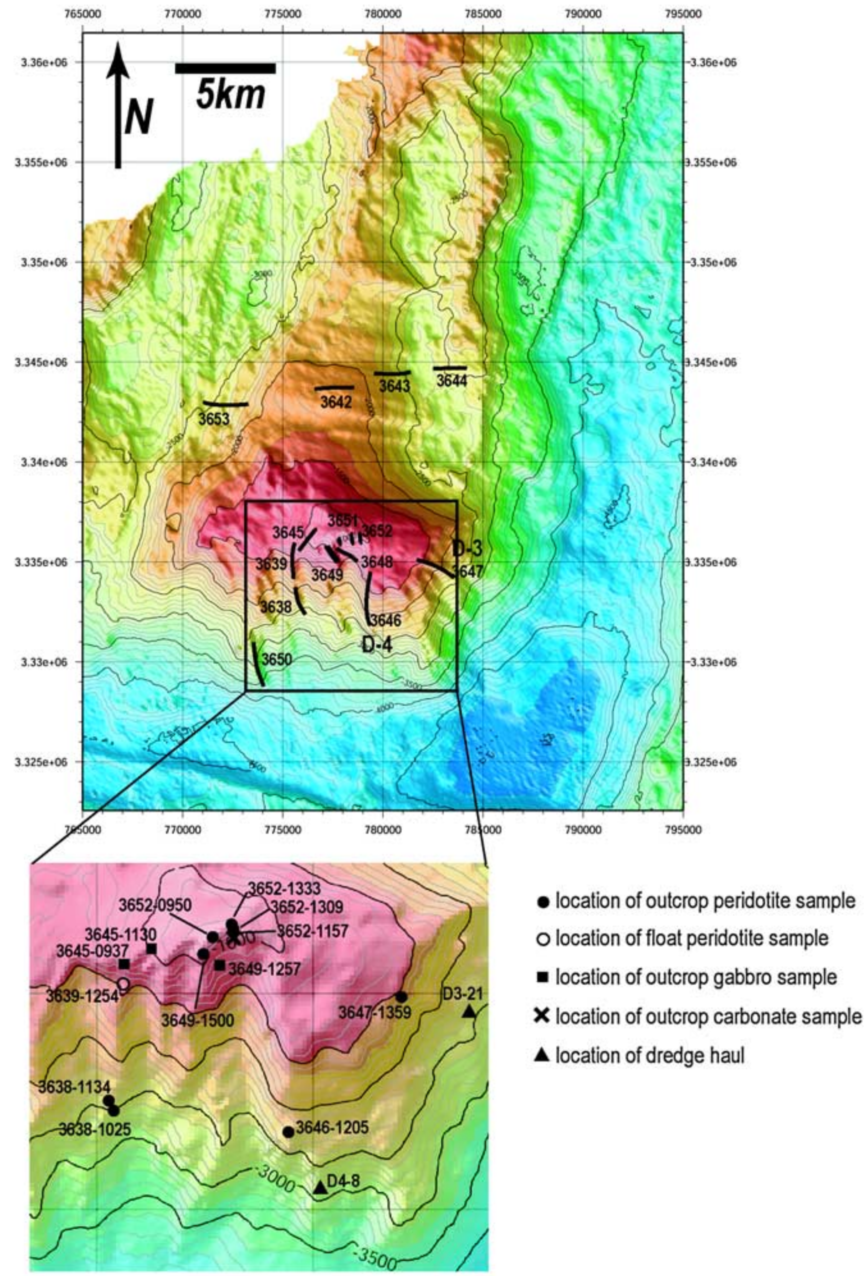

Figure 4. Map of Atlantis Massif showing locations of *Alvin* dive tracks, successful rock dredges (D3 and D4), and the location of several samples with detailed study reported in this work.

ples contain significant deformation textures, and are thus not included in this analysis.

4.1. Ductile Deformation

4.1.1. Peridotite

4.1.1.1. Crystal-Plastic Deformation

[10] Earliest formed fabrics preserved in peridotite samples consist of coarsely recrystallized olivine (recrystallized grain size = 0.5 mm to 2 mm) and subhedral pyroxene that contains bent cleavage and/or undulose extinction. Olivine grains have equant to irregular shapes, and grain boundaries meet at approximately 120°. Some grains display serrate margins indicative of recrystallization by high-temperature grain boundary migration [*Hirth and Tullis*, 1992]. Olivine crystals generally display undulose extinction and deformation bands, suggesting overprint by minor lower temperature strain. These textures are similar to medium to

Table 1. Locations and Depths of *Alvin* Samples Collected During the MAVEL 2000 Cruise That Are Used in This Study

Sample	Type	Depth	Latitude, N	Longitude, W
3638-1009	serpentinite	2545	30° 5.4241′	42° 8.3532′
3638-1025	serpentinite	2526	30° 5.4301′	42° 8.3445′
3638-1029	serpentinite	2526	30° 5.4301′	42° 8.3445′
3638-1134	serpentinite	2449	30° 5.5156′	42° 8.4328′
3638-1222	serpentinite	2366	30° 5.56′	42° 8.4565′
3638-1407	serpentinite	2015	30° 6.0141′	42° 8.416′
3638-1449	serpentinite	1918	30° 6.0433′	42° 8.4397′
3639-1254	serpentinite	1474	30° 6.9554′	42° 8.4061′
3639-1255	serpentinite	1474	30° 6.9554′	42° 8.4061′
3639-1256	serpentinite	1474	30° 6.9554′	42° 8.4061′
3639-1319	metaperidotite	1416	30° 7.0285′	42° 8.3209′
3639-1415	gabbronorite	1189	30° 7.2553′	42° 8.1716′
3641-1544	carbonate	1794	30° 10.4607′	42° 6.5897′
3641-1549	carbonate	1794	30° 10.458′	42° 6.5878′
3642-1130	basalt	1787	30° 10.4547′	42° 6.5978′
3642-1131	basalt	1787	30° 10.4547′	42° 6.5978′
3642-1308	serpentinite	1751	30° 10.2972′	42° 6.994′
3642-1309	serpentinite	1751	30° 10.2972′	42° 6.994′
3642-1310	serpentinite	1751	30° 10.2972′	42° 6.994′
3644-1125	pillow lava	2928	30° 10.904′	42° 2.1359′
3644-1520	pillow lava	2624	30° 10.9127′	42° 2.7921′
3645-0937	oxide gabbro	1267	30° 7.1438′	42° 7.9476′
3645-1032	metagabbro	1065	30° 7.3143′	42° 7.8699′
3645-1130	unknown	978	30° 7.337′	42° 7.8425′
3645-1159	serpentinite	957	30° 7.3549′	42° 7.8263′
3645-1225	serpentinite	955	30° 7.3543′	42° 7.8195′
3645-1227	peridotite	955	30° 7.3543′	42° 7.8195′
3645-1353	carbonate	817	30° 7.5708′	42° 7.534′
3646-1000	serpentinite	2507	30° 4.8742′	42° 6.0025′
3646-1045	gabbro	2466	30° 4.8726′	42° 5.9776′
3646-1205	serp-mylonite	2327	30° 4.9288′	42° 6.0286′
3646-1238	serpentinite	2255	30° 4.9797′	42° 6.0579′
3646-1328	gabbro	2043	30° 5.3364′	42° 5.9975′
3646-1409	serpentinite	1790	30° 5.665′	42° 6.0106′
3646-1452	gabbro	1657	30° 6.0076′	42° 6.0454′
3646-1459	gabbro	1578	30° 6.0228′	42° 6.0025′
3647-1158	limestone	1960	30° 6.8444′	42° 3.7532′
3647-1201	serpentinite	1960	30° 6.8444′	42° 3.7532′
3647-1208	metagabbro	1951	30° 6.8823′	42° 3.8154′
3647-1246	metagabbro	1862	30° 6.9235′	42° 3.849′
3647-1255	metagabbro	1862	30° 6.9235′	42° 3.849′
3647-1323	mylonite	1755	30° 7.0068′	42° 3.9211′
3647-1345	metagabbro	1661	30° 7.0913′	42° 4.0511′
3647-1359	metavolc	1623	30° 6.996′	42° 4.0499′
3648-1334	peridotite	1084	30° 7.2206′	42° 7.0488′
3648-1424	gabbro	1035	30° 7.2704′	42° 7.1869′
3648-1534	peridotite	947	30° 7.3045′	42° 7.2677′
3648-1545	breccia	920	30° 7.3045′	42° 7.2055′
3649-0924	serpentinite	1612	30° 6.6182′	42° 7.0351′
3649-1014	serpentinite	1521	30° 6.6772′	42° 7.0618′
3649-1108	gabbro	1423	30° 6.7459′	42° 7.0861′
3649-1149	carbonate	1300	30° 6.8488′	42° 7.1247′
3649-1257	gabbro	1188	30° 6.9689′	42° 7.1352′
3649-1359	serpentinite	1058	30° 7.1199′	42° 7.1676′
3649-1500	serpentinite	954	30° 7.2861′	42° 7.1819′
3650-1019	serpentinite	3056	30° 4.0168′	42° 9.634′
3650-1347	dikes	3000	30° 4.2485′	42° 9.588′
3651-1252	serpentinite	792	30° 7.4068′	42° 6.9685′
3652-0853	gabbro	874	30° 7.4339′	42° 7.1352′
3652-0905	serpentinite	863	30° 7.4393′	42° 7.1247′
3652-0938	oxide gabbro	795	30° 7.4647′	42° 7.1321′

Table 1. (continued)

Sample	Type	Depth	Latitude, N	Longitude, W
3652-0950	serpentinite	775	30° 7.4642′	42° 7.1004′
3652-1002	breccia/congl	732	30° 7.4588′	42° 7.1464′
3652-1123	serp+gabbro	890	30° 7.5844′	42° 6.7521′
3652-1157	conglomerate	832	30° 7.6011′	42° 6.7514′
3652-1203	serpentinite	834	30° 7.6028′	42° 6.7589′
3652-1226	serpentinite	805	30° 7.6028′	42° 6.7589′
3652-1245	unknown-mica	775	30° 7.6406′	42° 6.7894′
3652-1309	serpentinite	777	30° 7.6374′	42° 6.8012′
3652-1333	peridotite	790	30° 7.7116′	42° 6.7303′
3653-1210	vesicular bas	1642	30° 10.2074′	42° 7.9171′
3653-1355	metabasalt	1718	30° 10.2501′	42° 8.8664′
3653-1433	metabasalt	1801	30° 10.1706′	42° 9.0947′

coarse grained peridotite sampled from the Kane fracture zone that are thought to be deformed at shallow mantle conditions at temperatures >775°C [*Jaroslow et al.*, 1996].

[11] Coarsely recrystallized olivine fabrics are overprinted by thin (<5 cm) shear zones preserved in samples 3638-1025, 3639-1255, D4-3 and D4-5 (Figure 5a). Recrystallized olivine grain size ranges from 0.1 mm to 0.3 mm and generally fines toward the center of shear zones. Olivine neoblasts are equant in shape with ~120° grain boundary intersections, and have a moderately strong crystallographic preferred orientation as determined by optical inspection with a retardation plate. Remnant olivine porphyroclasts have strong

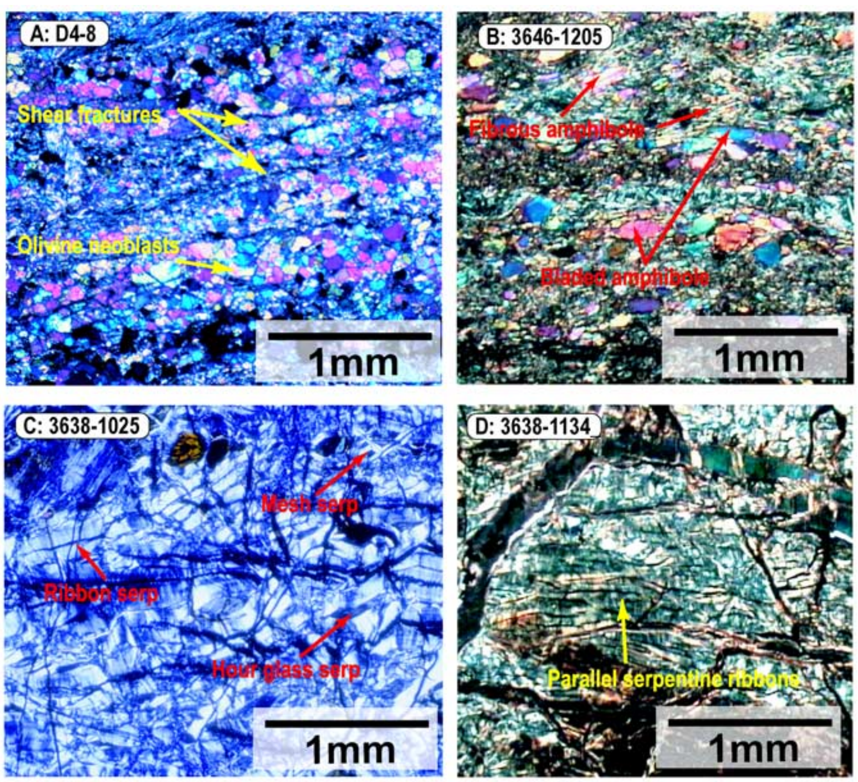

Figure 5. Photomicrographs of microstructures and serpentinization textures in peridotite. (a) D4-8: Peridotite mylonite deformed at granulite grade conditions; olivine is deformed by crystal-plastic flow and grain size reduced by dynamic recrystallization; brittle shear fractures with minor offset are parallel to the mylonitic foliation. (b) 3645-1205: Metasomatised peridotite schist; schistose foliation is defined by fibrous and bladed amphibole. (c) 3638-1025: Serpentinite with a combination of mesh, hourglass, and weak ribbon texture. (d) 3638-1134: Ribbon texture serpentine; ribbon serpentine is a dilational texture that defines the anastomosing outcrop foliation at Atlantis Massif.

patchy undulose extinction, deformation bands, are commonly elongate parallel to the foliation, and have asymmetric tails of finely recrystallized olivine. Orthopyroxene and clinopyroxene are present as porphyroclasts that contain bent cleavage and kink bands. Macroscopic foliation is defined by elongate bands of similar-sized olivine neoblasts. These textures are similar to those of peridotite mylonites described by *Jaroslow et al.* [1996] from the Kane fracture zone, which they suggest were deformed >600°C (near the brittle-ductile transition for olivine).

[12] Granulite-grade shear zones described above are overprinted in several samples by amphibolite-grade deformation in which olivine deforms by crystal plasticity but pyroxene has been altered to amphibole. The recrystallized grain size of equant olivine neoblasts ranges from 0.01 mm to 0.04 mm. Amphibole is colorless to very-pale brown and typically pseudomorphs clinopyroxene crystals. Microprobe mineral analyses indicate that the amphibole is tremolitic to weakly aluminous hornblende (Type I amphiboles discussed below). Amphibole appears in shear zones as porphyroclasts or fine-grained foliated aggregates. In sample 3638-1025, amphibole porphyroclasts are surrounded by aggregates of fine-grained elongate amphibole with dimensions ~ 0.01 mm by 0.05 mm. Straight grain boundaries are aligned parallel to and partially define the macroscopic foliation. Fine-grained amphibole is located in asymmetric pressure shadow tails of amphibole porphyroclasts or as continuous bands containing stretched and boudinaged amphibole porphyroclasts.

4.1.1.2. Diffusive Mass Transfer Deformation

[13] Several peridotite samples contain shear zones with a strong schistose foliation defined by parallel aligned bladed amphibole that replaced primary olivine and pyroxene (Figure 5a). Shear is indicated by the presence asymmetric pressure shadow tails on porphyroclasts. Bladed amphiboles are generally euhedral to subhedral, strain-free or very weakly strained, and have textures distinctly different from the amphibole pseudomorphs of clinopyroxene described above. Compositions of bladed amphiboles determined by electron microprobe are aluminous hornblende (approximately 1.8 cations of Al per formula; Type II amphiboles as described below), have variably high sodium content, and are commonly titanium rich (up to 4 weight% TiO_2). Within several such shear zones, primary peridotite minerals have been almost completely altered to amphibole and chlorite. Similar mineral assemblages in ophiolitic peridotites are termed blackwall horizons, where amphibole, tremolite and talc are grown in a metamorphic "mixing zone" in fault contact between the ultramafic ophiolite and continental rocks [*Chidester*, 1962; *Frost*, 1975]. Bladed amphibole shear zones contain accessory minerals including ilmenite, apatite, zircon, and/or monazite, and may also have small pockets (<1 mm) of plagioclase. Apatite commonly displays undulose extinction, subgrain boundaries and neoblasts. In general, samples with the greatest degree of blackwall-type alteration and/or metasomatism contain the largest concentrations of zircon and apatite. Sample 3646-1205, which has been almost completely altered to amphibole, contains over 50 zircon crystals in a single thin section (5 cm by 8 cm). Shear zones containing significant quantities of incompatible trace element-rich minerals and "blackwall" mineral assemblages suggest that strain was localized into zones of reaction between peridotite and highly evolved gabbro or hydrothermal fluids in contact with gabbroic magma.

4.1.2. Gabbro

[14] Deformation textures in gabbro samples indicate a down-temperature path of shear deformation in which fine-grained shear zones with amphibolite grade mineral assemblages overprint coarser-grained zones with granulite grade minerals. Earliest formed deformation fabrics consist of coarse-grained recrystallized plagioclase ranging in grain size from 0.2 mm to 0.5 mm. Plagioclase neoblasts are equant to slightly elongate parallel to the foliation with equilibrated grain boundaries that meet at ~120° angles, have a moderate to strong CPO based on optical inspection with a retardation plate, have patchy undulose extinction with local sub grain formation, and contain late-formed deformation twins. Pyroxene in coarse-grained shear zones is porphyroclastic with large orthopyroxene and clinopyroxene crystals up to 3 cm in diameter; these grains show moderate internal strain and are sometimes rimmed by neoblasts ranging in size from 0.2 mm to 0.6 mm (Figure 6a). One peridotite sample preserves a thin (2 cm wide) sheared gabbro dike in which plagioclase has recrystallized to grain size ranging from 0.001 mm to 0.01 mm, and pyroxene neoblasts range from 0.005 mm to 0.01 mm in diameter.

[15] Amphibolite grade mylonitic shear zones consist of recrystallized plagioclase with neoblast grain size ranging from 0.02 mm to 0.08 mm, and brown and green amphibole porphyroclasts rimmed by 0.1 mm amphibole neoblasts that define

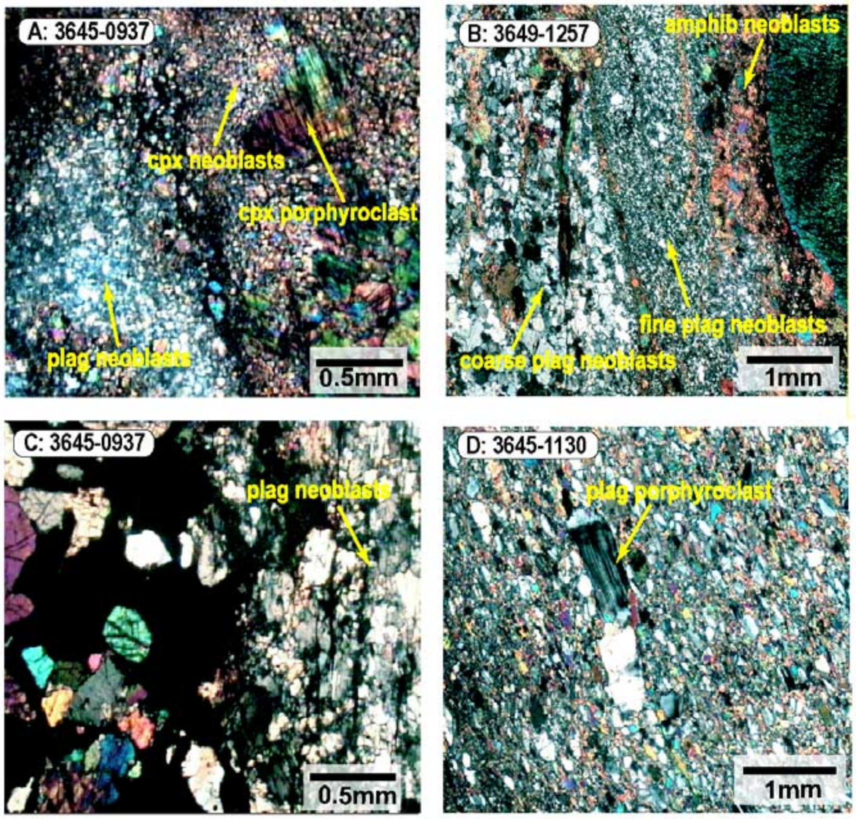

Figure 6. Photomicrographs of microstructures in gabbro. (a) 3645-0937: Gabbro mylonite deformed at granulite-grade conditions; sample displays core and mantle texture with clinopyroxene neoblasts surrounding a clinopyroxene porphyroclast and finely recrystallized plagioclase neoblasts. (b) 3649-1257: Gabbro mylonite deformed at amphibolite-grade; image contains a shear zone with finely recrystallized plagioclase within coarser recrystallized plagioclase neoblasts; cpx porphyroclast is rimmed by amphibole neoblasts. (c) 3645-0937: Fe-Ti oxide-rich shear zone in gabbro, opaque minerals are ilmenite and magnetite and contain porphyroclasts of clinopyroxene and plagioclase; fine-grained plagioclase neoblasts on the right side of image contain through-running shear fractures. (d) 3645-1130: Gabbro schist; plagioclase porphyroclasts have been rotated into schistose foliation but retain igneous twins and zoning, indicating only minor internal plastic deformation; matrix is fine-grained, fibrous aluminous amphibole with strong shape preferred orientation.

asymmetric pressure shadow tails. Grain boundaries in plagioclase neoblasts are equilibrated and grains show no subsequent deformation. Plagioclase neoblasts generally have straight to gently curved grain boundaries between one another, but grain boundaries between neoblasts and porphyroclasts are highly serrate, suggesting low-temperature grain boundary migration recrystallization [*Hirth and Tullis*, 1992; *Tullis and Yund*, 1987]. Amphibolite shear zones in sample 3649-1257 cut the foliation of granulite shear zones at angles less than 10°.

[16] Mylonitic shear zones in several gabbro samples are rich in Fe-Ti oxides and apatite, and several also contain zircon and/or sphene (Figure 6c). Granulite-grade shear zones in sample 3645-0937 contain magnetite grains with undeformed ilmenite exsolution lamellae, suggesting that penetrative deformation ceased prior to oxy-exsolution of spinel ilmenite from ulvospinel. Apatite in most samples has been deformed by crystal plasticity, and displays undulose extinction, subgrain development and recrystallized neoblasts.

[17] Several gabbro samples consist of vein-like zones of mostly strain-free, brown to green pleochroic amphibole with strong shape preferred orientation that defines a schistose foliation. The matrix of sample 3645-1130 is formed of brown amphibole with average length of 0.05 mm by 0.01 mm width, and contains elongate plagioclase porphyroclasts ranging from 0.05 mm to 0.1 mm that are parallel to the schistose foliation. Several plagioclase porphyroclasts retain igneous zoning and twins, indicating limited crystal plastic

deformation. This texture is very similar to deformation textures in metagabbro hypothesized by *Brodie and Rutter* [1985] to have formed by diffusive mass transfer and grain boundary sliding.

4.2. Serpentinization Fabrics

[18] Granulite- and amphibolite-grade deformation textures in peridotite are overprinted by static serpentinization. Serpentinization of peridotite occurs in the presence of water at temperatures below 500°C, and involves hydration of olivine and pyroxene to serpentinite group phyllosilicates [*O'Hanley*, 1996]. Most serpentinite samples display a combination of mesh, hourglass, and ribbon textures (Figure 5c). Mesh texture serpentinite, in which texture is dominated by cells containing distinct rim and core domains, forms under static conditions in which water infiltrates along passive tension fractures [*O'Hanley*, 1992]. Hourglass texture, in which cell rims and cores are not distinct mineral domains, forms when peridotite is actively fractured to permit water infiltration [*O'Hanley*, 1996]. Ribbon texture serpentinite is a variant of hourglass serpentinite that is formed when closely spaced sets of parallel dilational fractures are filled by serpentine veins between 0.5 and 2 mm wide. Serpentine ribbons define a strong foliation in most Atlantis Massif serpentinite samples, and is commonly oriented parallel to foliation formed during crystal-plastic deformation (Figure 5d). Anastomosing foliation visible in Atlantis Massif serpentinite outcrops is defined by ribbon serpentine. Although this fabric is pervasive at Atlantis Massif, it appears to be dominantly dilational and represents little or no shear strain accommodation.

4.3. Semibrittle Deformation Fabrics

[19] Ductile deformation and serpentinization fabrics are overprinted by complex semibrittle shear zones that exhibit textures indicating strain accommodation by a combination of diffusive mass transfer and cataclasis. Semibrittle deformation fabrics are strongly developed only in peridotite samples, and rarely appear in gabbro.

4.3.1. Amphibole-Chlorite Schist

[20] Amphibole-chlorite schist shear zones consist of fine-grained fibrous amphibole and chlorite (and rare talc) with little or no internal crystal plastic strain defining a strong schistose foliation (Figure 7a). Fibrous amphiboles are low-aluminum tremolite (Type III amphiboles, see mineral chemistry section, below) and range in size from 1 mm to <0.0001 mm. Mats of fibrous amphibole contain brittlely deformed porphyroclasts of serpentinite and bladed high-Al hornblende. Bladed hornblende porphyroclasts are commonly fractured along cleavage planes, stretched and rotated into the schistose foliation with tails of fibrous amphibole, indicating shear deformation (Figure 7b). Serpentinite porphyroclasts with intact mesh texture appear to have been incorporated into amphibole-chlorite schist by brittle fracture of a preexisting serpentinized peridotite (Figure 7c). Many serpentinite porphyroclasts have serrate boundaries and may be "fish" shaped. Both of these fabrics are presumed to have formed as a result of modification along the porphyroclast margins due to reaction with surrounding tremolite and/or fluids during intense shear deformation. The presence of serpentinite porphyroclasts whose veining structure is cut by fibrous tremolite shear zones requires that the shear zone formed after serpentinization of peridotite. These shear zones resemble metaperidotite "fault schists" described by *Escartín et al.* [2003] from an oceanic detachment fault at 15°N on the Mid-Atlantic Ridge. Semibrittle shear zones consisting of intensely altered peridotite suggest strain localization via reaction softening processes.

4.3.2. Carbonate-Amphibole Schist

[21] Several Atlantis Massif metaperidotite samples contain schistose veins of intercalated aragonite and fibrous amphibole (Figure 7d). Strain-free aragonite crystals are fibrous and interlayered with tremolite. This fabric is presumed to have formed during shear deformation by processes similar to the tremolite-chlorite schist shear zones described above, but in the presence of fluids with high Ca and CO_2 activity to cause aragonite precipitation. Cross-cutting relations are not present in any samples to determine the timing of carbonate-amphibole schist relative to other semibrittle deformation.

4.4. Brittle Deformation Fabrics

4.4.1. Brittle Deformation of Peridotite

[22] Brittle deformation of peridotite and metaperidotite is characterized by a combination of shear-bounded phacoids of amphibole-chlorite schist or serpentinite (Figure 8a), and fine-grained cataclasite (Figure 9). The interior of phacoids may also show cataclastic deformation, but to a lesser degree

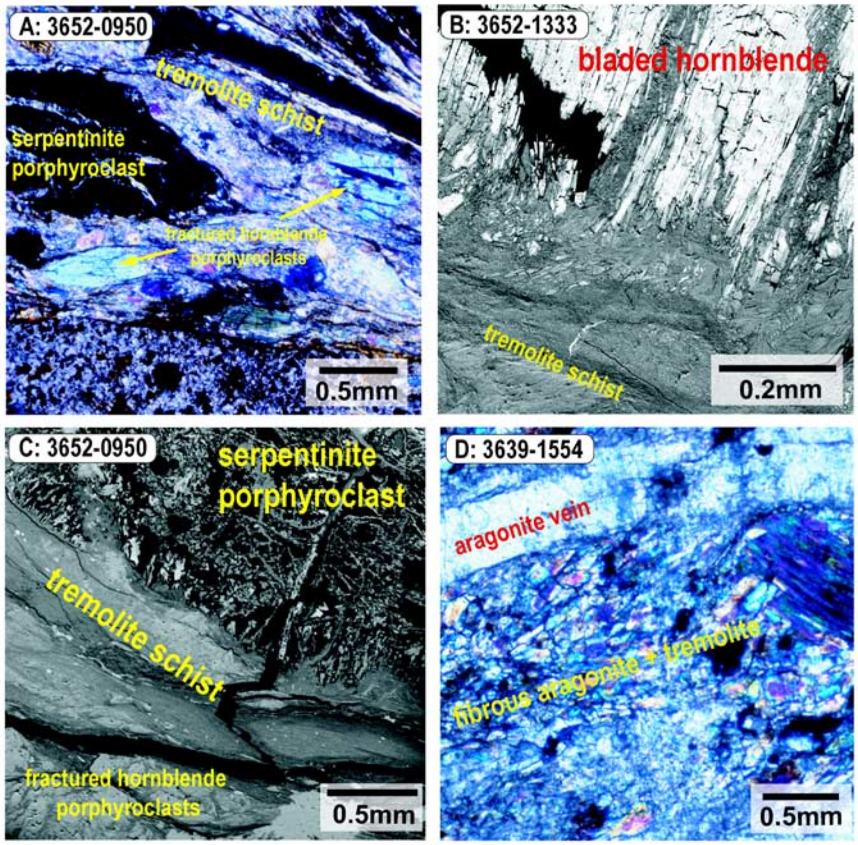

Figure 7. Photomicrographs of semibrittle deformation textures in peridotite. (a) 3652-0950: Tremolite-chlorite schist containing porphyroclasts of tabular aluminous amphibole and serpentinite. (b) 3652-1333: Margin of semibrittle tremolite-chlorite schist shear zone; porphyroclast of aluminous amphibole is cataclastically deformed with fragments pulled into shear zone and partially altered to tremolite and chlorite. Fabric resembles paracrystalline microboudinage. (c) 3652-0950: Margin of serpentinite porphyroclast in tremolite-chlorite shear zone; veining texture in serpentinite is intact and cut by tremolite schist, indicating that serpentinization of peridotite preceded formation of shear zone. (d) 3639-1554: Tremolite-carbonate schist containing intercalated fibrous tremolite and aragonite and an aragonite vein oriented parallel to the foliation.

than the bounding shear zones. Outcrops of brittlely deformed peridotite viewed with submersibles contain closely spaced (<1 cm) fractures oriented either randomly or subparallel to foliation, and contain breccia clasts between 5–20 cm. Weak to moderately well-developed shear foliation has a subhorizontal to moderately dipping (up to 30°) orientation.

4.4.2. Ophicalcite Fracture Fill

[23] Basement rocks exposed along the southern wall of the massif are infiltrated by veins, neptunic dikes and dikelets of carbonate and carbonate-matrix breccia. The carbonate originated as biogenic calcareous mud composed of foraminifer and coccolith microfossils (Figure 8b) that accumulated on the seafloor and was mobilized into fracture systems. Calcareous mud was lithified by interaction with serpentinization-derived fluids [*Schroeder et al.*, 2002]. Minor late-stage brittle deformation of peridotite, gabbro and lithified carbonate results in networks of shear fractures and minor faults recorded in dives 3649 and 3652 that are filled with carbonate mud and carbonate-matrix breccia (Figures 8c and 8d). Injection of seafloor-derived carbonate mud into shear fractures suggests that seawater infiltrated fracture systems during brittle deformation and unroofing of Atlantis Massif.

4.4.3. Brittle Deformation of Gabbro

[24] Shear fractures with minor offset are present in several gabbro samples, but none of the gabbro samples collected from Atlantis Massif have expe-

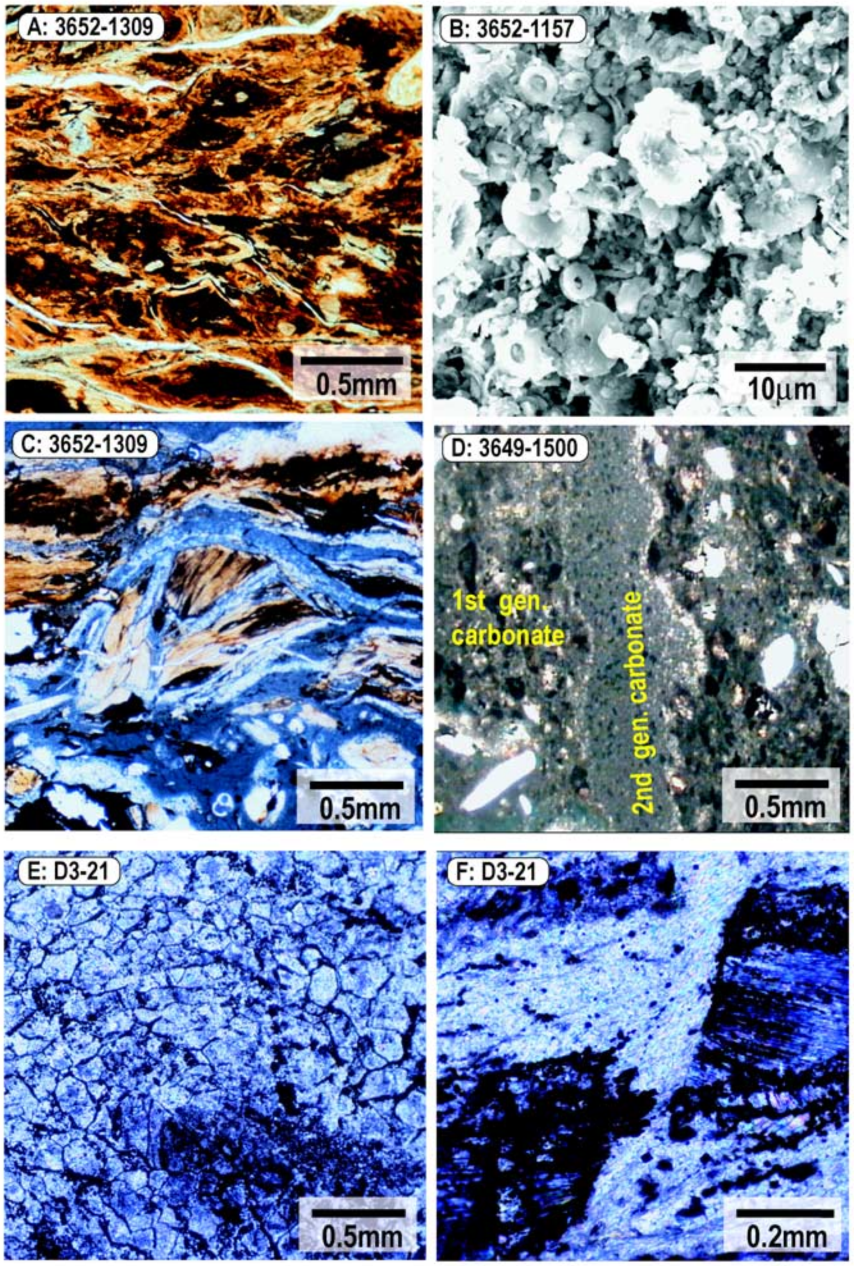

Figure 8. Photomicrographs of brittlely deformed peridotite and carbonate. (a) 3652-1309: Metaserpentinite cataclasite from the upper portion of massif south wall; phacoids of semibrittle, tremolite-chlorite schist are cut by anastomosing brittle shears. (b) 3652-1157: Backscattered electron image of the matrix of a carbonate breccia sample: fine-grained matrix is composed of biogenic material including coccolith plates and foraminifer fragments. (c) 3652-1309: Cataclastic metaserpentinite in which shear fractures are filled with fine-grained, lithified carbonate mud. (d) 3649-1500: Multiple stages of fracturing and carbonate mud injection in carbonate breccias; the first generation of carbonate mud is cut by a dilational fracture filled with second generation carbonate mud. (e) D3-21: Static talc alteration; mesh texture serpentinite (mesh cells outlined by remnant magnetite) is completely replaced by fine-grained talc. (f) D3-21: Talc alteration during dilational brittle fracturing; schistose talc is aligned parallel to opening direction of fracture that offsets altered tremolite grains.

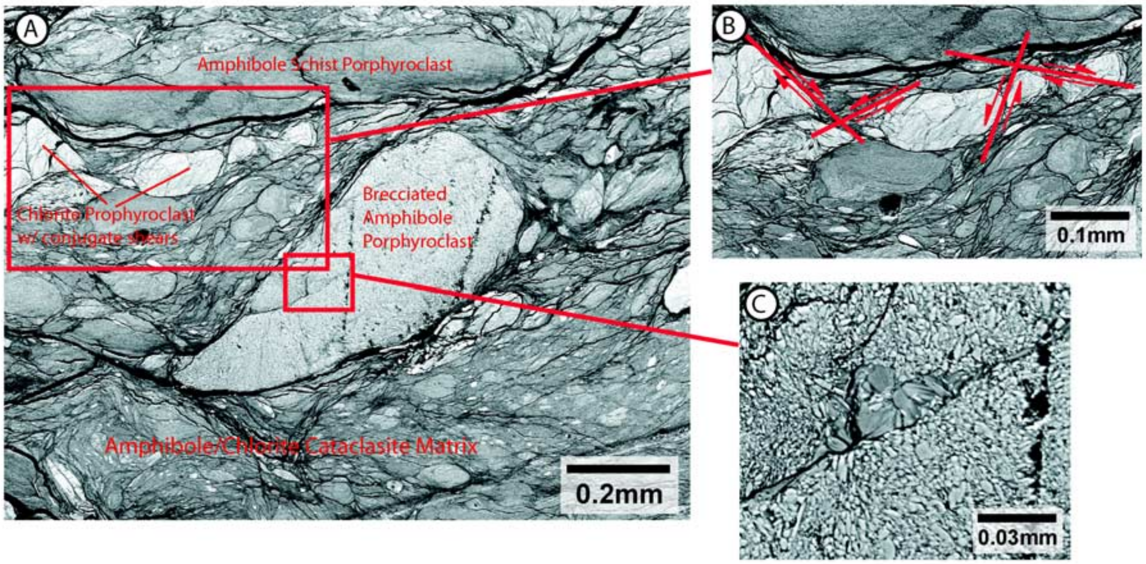

Figure 9. Backscattered electron images of partially oriented (foliation is subhorizontal, but full orientation is not known) sample 3652-1309; metaserpentinite cataclasite. (a) Phacoidal porphyroclasts of aluminous amphibole, tremolite-chlorite schist, and chlorite in matrix of fine-grained tremolite-chlorite cataclasite. (b) Conjugate fracturing of iron-rich chlorite porphyroclasts. (c) Close-up of large amphibole porphyroclasts; porphyroclast is formed of very fine-grained amphibole breccia with secondary cohesion.

rienced a significant degree of cataclastic deformation. Shear fractures in some gabbro samples are filled with undeformed hornblende veins, suggesting that minor brittle deformation occurred under amphibolite facies conditions.

4.5. Talc Overprint of Peridotite and Serpentinite

[25] Many peridotite, serpentinite and metaperidotite samples collected from near ($\leq$10 m) the upper surface of Atlantis Massif have been nearly completely altered to fine-grained talc. Talc with grain size less than 0.01 mm overgrows serpentine, orthopyroxene, amphibole, and chlorite. Talcified serpentinite samples commonly display very fine magnetite crystals that outline former serpentine mesh cells (Figure 8a), suggesting talc replacement occurred at least locally under static conditions. Other samples contain schistose talc grains orientated parallel to the opening direction of dilational shear fractures (Figure 8b), suggesting alteration to talc during minor brittle deformation.

4.6. Cross-Cutting Relations and Evolution of Deformation Fabrics

[26] The progression of deformation fabrics and mineral assemblages in peridotite are as follows:

[27] 1. Granulite-grade deformation fabrics and mineral assemblages are overprinted by amphibolite-grade mineral assemblages and deformation fabrics.

[28] 2. Static serpentinization overprints granulite- and amphibolite-grade mineral assemblages.

[29] 3. Semibrittle deformation overprints amphibolite grade deformation fabrics and serpentinization textures.

[30] 4. Brittle deformation overprints semibrittle deformation and serpentinization fabrics.

[31] 5. Talc alteration overprints all fabrics and mineral assemblages.

[32] The progression of deformation fabrics in gabbro samples is as follows:

[33] 1. Granulite-grade deformation fabrics and mineral assemblages are overprinted and cut by amphibolite-grade deformation fabrics.

[34] 2. Minor brittle deformation cuts amphibolite- and granulite-grade deformation fabrics.

[35] 3. Static greenschist and zeolite grade alteration overprints all mineral assemblages.

[36] This down-temperature pattern of deformation and alteration is consistent with tectonic denudation

Table 2. Descriptive Deformation Intensity Scales

Deformation Intensity	Ductile Deformation	Semibrittle Deformation	Brittle Deformation
0: Undeformed	no observed deformation	no observed deformation	no observed deformation
1: Slight deformation	weak foliation, no grain size reduction	minor fracturing and syn-tectonic mineral growth with weak preferred orientation (<40% of new minerals oriented with the long axis <20° from shear foliation)	minor fracturing; no significant grain size reduction
2: Weak deformation	strongly foliated, no significant grain size reduction	minor fracturing and minor mineral growth with moderate preferred orientation (40–70% of newly formed minerals oriented with the long axis <20° from shear foliation)	moderate fracturing; no significant grain size reduction
3: Moderate deformation	porphyroclastic (proto) mylonite, <20% grain size reduction	moderate fracturing and moderate mineral growth with strong preferred orientation confined to shear zone or vein (>70% of newly formed minerals oriented with the long axis <20° from shear foliation)	dense anastomosing fracturing and incipient breccia (<20% matrix)
4: Strong deformation	mylonite, 20–70% grain size reduction of all phases	intense fracturing and pervasive mineral growth with strong preferred orientation (>70% of newly formed minerals oriented with the long axis <20° from shear foliation) confined to shear zones or veins	well-developed fault brecciation; rotation of clasts (20%–70% matrix)
5: Intense deformation	ultramylonite, >70% grain size reduction of all phases	intense fracturing and pervasive mineral growth with strong preferred orientation (>70% of newly formed minerals oriented with the long axis <20° from shear foliation) affecting entire sample	cataclasite (>70% matrix)

of lower-crustal and mantle rock by normal faulting [*Ehlers et al.*, 2001].

5. Spatial Distribution of Deformation Textures

[37] This analysis seeks to determine if the vertical distribution of deformation fabrics indicates brittle strain localization near the domal bathymetric surface of Atlantis Massif and includes (1) an estimate of the intensity of ductile, semibrittle, and brittle strain textures in each sample and (2) an estimate the structural depth beneath the domal surface each sample was collected along steep landslide scarp headwalls.

5.1. Strain Intensity

[38] We seek to evaluate the degree to which strain was localized into a particular horizon by assuming that the displacement along a shear zone is proportional to a qualitative rating of the intensity of the strain fabric in shear zones. Because of the nature of submersible sampling, it was not possible to determine the displacement along any shear zone. Fabric intensity is rated on a scale of none (0) to high (5) for ductile, semibrittle, and brittle deformation in each peridotite and gabbro sample. Intensity scale criteria are detailed in Table 2. The intensity scales for ductile and brittle deformation are modified from those used by shipboard scientists on ODP Leg 176 to describe deformation in gabbro from Hole 735B [*Dick et al.*, 1999]. The ductile scale is based on the percentage of grain size reduction due to dynamic recrystallization and recovery. The intensity of brittle deformation is based on the percentage of grain size reduction by fracturing and cataclasis. The limitation of these scales is that they require knowledge of the grain size prior to deformation. For samples that do not contain undeformed material outside a shear zone, predeformation grain size is estimated from porphyroclast size. Semibrittle/ductile deformation textures as described above are formed by a combination of cataclasis, diffusive mass transfer during growth of alteration minerals, and grain boundary sliding. Because of this, it was necessary to develop a site-specific deformation intensity scale that is based on both the degree of fracturing and the development of schistose fabric (Table 2).

5.2. Structural Depth Estimation

[39] The domal upper surface of Atlantis Massif is dissected along its southern flank by a series of scallop-shaped landslide scarps that face south into the transform valley (Figures 1 and 4). Most

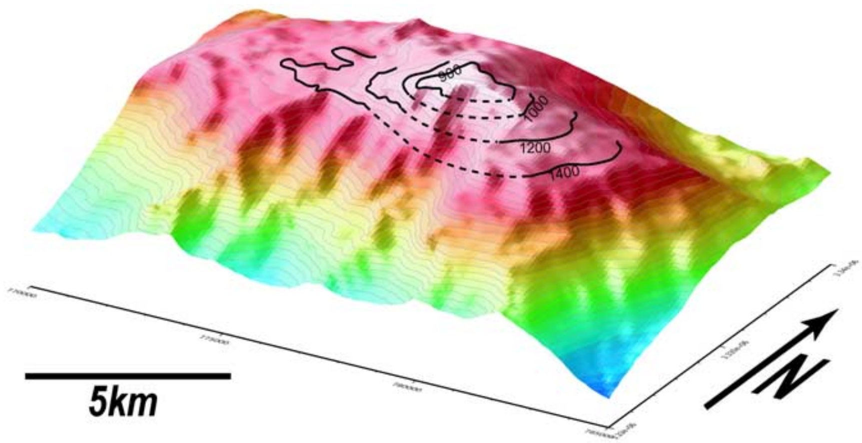

Figure 10. Three-dimensional minimum elevation perspective of Atlantis Massif south flank with minimum elevation structure contour estimates of the domal surface prior to mass wasting.

samples used in this study were collected from outcrops on the walls of these scarps. The headwalls of the scarps intersect the domal surface where it dips gently (<10°) south, approximately 2 km south of the massif summit. Assuming that the domal surface was continuous across the landslide scarps, it is possible to construct a minimum relief structure contour map of the undissected dome prior to mass wasting (Figure 10). An estimate of structural depth beneath this surface is made by subtracting the paleo-elevation (depth below sea level) of the bathymetric surface from the known sample depth (Table 3). It was only possible to estimate the structural depth of samples collected to water depths of approximately 2300 m along the south flank, which includes structural depths <520 m below the domal surface. This analysis assumes that the domal surface dipped downward (south) into the transform valley with a continuous radius of curvature. There are several possible scenarios for the morphology of inside corner highs along transform valley walls [*Blackman et al.*, 2004]. The error in estimated structural depth is likely least for samples collected from shallow levels near headwall scarps and greater for samples collected at greater depths. Structural depths less than 50 m are likely accurate to within ±5 m, depths between 50 m and 100 m are accurate to ±10 m, depths between 100–300 m are accurate to ±20 m, and depths greater than 300 m are accurate to ±50 m.

5.3. Strain Intensity Variation With Structural Depth

[40] Intensity of brittle, semibrittle and ductile strain fabrics are averaged over 10 m structural depth intervals by summing the intensity of all samples and dividing by the number of samples in that interval. Histograms of average strain fabric intensity versus structural depth reveal distinct patterns of strain localization (Figure 11). Ductile strain is not localized at any particular structural depth, but has relatively constant fabric intensity from directly beneath the domal surface to depths of over 520 m. Semibrittle and brittle strain of peridotite is concentrated within the upper 90 m beneath the domal surface. Several samples between 90 m and 10 m structural depth contain moderate to strong (intensity between 2 and 5) semibrittle strain fabrics and moderate brittle strain fabrics. The highest concentration of sampling is within the upper 10 m beneath the domal surface. The 15 samples in this interval have average semibrittle fabric intensity of 3.3 and average brittle fabric intensity of 2.7. All samples with extreme brittle strain (>4 intensity) were sampled within the upper 10 m beneath the domal surface. This pattern of concentrated semibrittle, intermediate temperature strain and brittle strain mirrors deformation texture patterns in continental metamorphic core complexes [*Spencer*, 1984; *Davis et al.*, 1986; *John*, 1987]. During tectonic denudation associated with continental metamorphic core complex development, strain is progressively localized from diffuse shear zones, into a narrow zone below the detachment fault [*Davis et al.*, 1986; *Spencer and Reynolds*, 1989]. Concentration of semibrittle schists in the upper 90 m beneath the surface mirrors concentration of similar "fault schists" within the upper 100 m beneath an oceanic detachment at 15°N on the Mid-Atlantic Ridge studied by *Escartín et al.* [2003]. This documented distribution of strain at

Table 3. Structural Depth and Deformation Intensity of Peridotite and Gabbro Samples Used in Statial Variation Analysis

				Peridotite Deformation Intensity		
Sample	Sample Depth	Surface Depth	Structural Depth	Ductile	Semibrittle	Brittle
3650-1019	3056		520	1	0	0
3638-1009	2545	2030	515	0	0	0
3638-1025	2526	2025	501	1	3	1
3638-1027	2526	2025	501	1	0	0
3638-1029	2526	2025	501	1	1	1
3638-1047	2525	2025	500	0	0	0
3638-1134	2449	2005	444	0	1	0
3638-1222	2366	1930	436	0	0	0
3638-1313	2226	1825	401	0	0	0
3649-0924	1612	1280	332	1	0	0
3638-1407	2015	1700	315	0	0	0
3638-1449	1918	1630	288	0	0	0
3649-0959	1523	1260	263	0	0	0
3639-1027	1646	1430	216	0	0	0
3639-1055	1615	1410	205	0	0	0
3639-1123	1550	1380	170	0	0	0
3648-1334	1084	920	164	0	0	0
3648-1403	1067	915	152	0	0	0
3645-0935	1267	1175	92	0	0	0
3652-1101	916	825	91	0	0	0
3649-1359	1058	975	83	2	3	3
3648-1534	947	870	77	0	1	0
3652-0905	863	790	73	1	1	1
3652-1123	890	820	70	2	2	1
3639-1355	1295	1230	65	1	0	0
3649-1432	1014	950	64	0	0	0
3646-1452	1657	1600	57	4	2	2
3646-1205	2327	2290	37	0	5	0
3652-1157	832	810	22	1	4	2
3651-1252	792	775	17	1	1	1
3646-1409	1790	1780	10	0	1	0
3639-1415	1189	1180	9	1	3	3
3646-1238	2255	2250	5	1	3	2
3652-0950	775	770	5	3	5	3
3652-1226	805	800	5	0	1	0
3645-1159	957		2	0	4	2
3645-1225	955		2	0	4	3
3647-1359			2	1	4	2
3645-1227	955		1	0	4	2
3642-1308	1751		0	2	3	3
3642-1309	1751		0	0	2	4
3642-1310	1751		0	0	2	2
3652-1002	732	732	0	1	3	4
3652-1245	775	775	0	0	5	2
3652-1309	777	777	0	2	5	5
3652-1333	790	790	0	2	4	4

				Gabbro Deformation Intensity		
Sample	Sample Depth	Fault Depth	Structural Depth	Ductile	Semibrittle	Brittle
3650-1347	3000		>500	2	1	1
3638-1134	2449	2005	444	5	0	0
3649-1108	1423	1240	183	4	0	1
3646-1045	2466	2300	166	1	1	0
3648-1424	1035	900	135	2	2	1
3646-1138	2393	2290	103	0	0	0
3645-0937	1267	1175	92	3	0	0
3649-1257	1188	1115	73	5	0	1
3646-1328	2043	2000	43	2	1	1

Table 3. (continued)

Sample	Sample Depth	Fault Depth	Structural Depth	Gabbro Deformation Intensity		
				Ductile	Semibrittle	Brittle
3646-1328	2043	2000	43	2	1	1
3652-1157	832	810	22	2	1	0
3645-1032	1065	1045	20	4	0	0
3652-0938	795	775	20	3	1	1
3645-1130	978	960	18	5	0	0
3639-1415	1189	1180	9	1	2	1

Atlantis Massif shows that the upper surface is a fault, and clearly supports the oceanic core complex hypothesis.

6. Mineral Chemistry and Thermometry

[41] The compositions of amphibole and chlorite from peridotite samples as well as amphibole and plagioclase from gabbro samples were measured to estimate temperature and chemical conditions during deformation. Mineral compositions were analyzed on polished, carbon-coated thin sections with a JEOL JXA-8900 five-spectrometer electron microprobe. Analytical procedures are detailed in Appendix A.

6.1. Gabbro Mineral Chemistry and Plagioclase-Hornblende Thermometry

[42] Deformation temperature estimates were made using the modified hornblende-plagioclase geothermometer [*Holland and Blundy*, 1994; *Dale et al.*, 2000] in highly deformed samples 3649-1257 and 3645-1130. Discussion of methods used to processes mineral chemistry data are detailed in Appendix A along with a discussion of error estimation. Representative amphibole and plagioclase analyses are listed in Table 4, and complete data, as well as thermometry calculations, are listed in the auxiliary material.[1]

[43] Sample 3649-1257 is a gabbro mylonite in which strain was accommodated dominantly by crystal-plastic deformation (dislocation creep) of plagioclase. The highest estimated temperatures in sample 3649-1257 (915°C) were calculated from analyses of weakly deformed brown hornblende near orthopyroxene porphyroclasts (Figure 12), suggesting low-strain or static hydration of pyroxene at high temperature. Estimated temperatures range from 750°C to 850°C within zones of coarsely recrystallized plagioclase (0.1 mm–0.4 mm) with serrate grain boundaries indicative of grain boundary migration recrystallization. Zones of finely recrystallized (0.02 mm–0.05 mm) polygonal plagioclase and associated amphibole yielded the lowest temperatures, ranging from 750°C–650°C. These relations suggest low-stress deformation at temperatures >900°C, followed by crystal-plastic deformation as temperature dropped to lower-granulite-grade conditions. Strain was progressively localized into narrow shear zones with finer recrystallized grain size as temperature dropped to middle-amphibolite grade.

[44] Sample 3645-1130 is a fine-grained, strongly foliated gabbro with plagioclase porphyroclasts contained within a fine-grained (0.02 mm–0.04 mm) matrix of brown pleochroic amphibole (Figure 13). Both plagioclase and amphibole crystals are strain-free, and the sample is interpreted to have been deformed by diffusive mass transfer with grain boundary sliding. The range of calculated temperatures in sample 3649-1257 (915°C to 673°C) and sample 3645-1130 (850°C–656°C) overlap. Temperature may therefore not be a factor in whether gabbro is deformed by crystal plasticity or diffusive mass transfer at amphibolite facies, and the exact strain localization mechanisms at Atlantis Massif may have been dependent on the availability of water and reactants transported through fracture networks.

6.2. Peridotite Mineral Chemistry

6.2.1. Amphibole Chemistry

[45] Three distinct populations of amphibole in peridotite samples are delineated on the basis of mineral chemistry and textural characteristics. Type I (in this classification) amphiboles are low-aluminum, calcic amphiboles (tremolite) that form pseudomorphs of pyroxene. Pseudomorphs

[1]Auxiliary material is available at ftp://ftp.agu.org/apend/gc/2004GC000728.

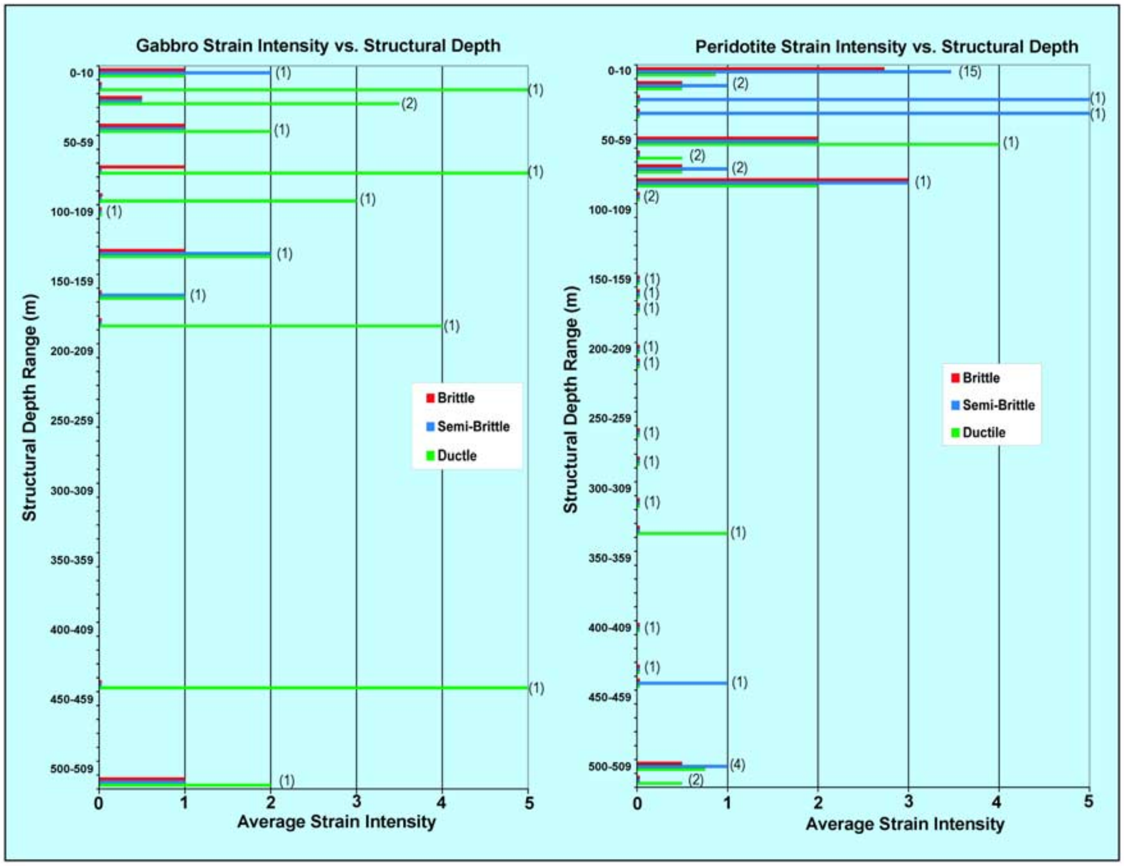

Figure 11. Histograms of average deformation intensity (sum of intensity estimates divided by the number of samples) versus structural depth beneath the domal surface of Atlantis Massif. Data show no strong correlation between structural depth and intensity of ductile deformation. Semibrittle deformation in peridotite is concentrated in the upper 90 meters below the domal surface, and brittle deformation is concentrated within the upper 10 meters below the domal surface.

often preserve deformation textures of pyroxene including undulose extinction and kink bands. Type 1 amphiboles are associated with olivine, orthopyroxene and chromite, and likely formed by hydration of clinopyroxene when peridotite was infiltrated by water along brittle fractures during amphibolite facies deformation. Representative analyses of type I, II and III amphiboles are listed in Table 5 (all analyses are listed in the auxiliary material[1]).

[46] Type II amphibole has high aluminum and sodium (pargasite-hornblende composition) and forms bladed, tabular crystals that either overgrow the rock matrix or fill voids in vein-like structures. Tabular crystals are generally aligned parallel to foliation and appear to have grown concurrently with crystal-plastic deformation of olivine. Mineral associations of Type II amphiboles include olivine, orthopyroxene, and in some samples ilmenite, apatite, zircon and monazite. Growth of pargasitic hornblende in peridotite requires metasomatic addition of aluminum and sodium, and the presence of apatite, zircon, monazite and ilmenite suggest enrichment in iron and incompatible trace elements. It is therefore likely Type II amphiboles formed in response to infusion of an evolved gabbroic melt or fluids that were in communication with highly evolved gabbroic magma.

[47] Type III amphiboles are generally fine-grained (<0.05 mm), elongate fibrous crystals of tremolitic composition (with variable minor Al and Na content). Type III amphiboles form the bulk of semibrittle, tremolite-chlorite schist shear zones discussed above, and have been analyzed in samples 3652-1309, 3652-0950, and 3645-1259. Mineral associations include chlorite, serpentine, talc and hematite, and in some samples ilmenite,

10.1029/2004GC000728

Table 4. Selected Analyzed Amphibole and Plagioclase Compositions From Gabbro Samples[a]

	Amphibole Sample 3645-1130 Analysis Number							Amphibole Sample 3649-1257 Analysis Number						
	1130a1	1130a13	1130a18	1130ab5	1130ab13	1130ac10	1130ac7	1257A2	1257A22	1257B3	1257B12	1257D7	1257E4	1257E12
SiO_2	49.98	50.61	49.81	48.12	47.32	46.68	43.34	44.88	48.64	54.27	57.84	52.49	50.35	50.08
Al_2O_3	7.41	7.01	7.80	8.27	10.24	11.14	12.81	9.80	6.59	28.61	24.27	1.78	6.41	4.96
TiO_2	0.70	0.68	0.76	1.36	1.47	1.41	1.40	1.01	1.13	0.01	0.03	0.17	0.65	0.76
Cr_2O_3	0.11	0.20	0.17	0.18	0.11	0.13	0.19	0.02	0.03	0.00	0.00	0.11	0.02	0.03
MgO	17.32	17.39	17.41	16.29	16.53	13.72	12.61	12.69	14.17	0.01	0.94	23.89	15.81	15.43
FeO	8.91	8.70	8.95	9.81	8.94	12.57	14.39	15.77	13.75	0.26	0.93	17.12	12.90	12.05
MnO	0.08	0.10	0.07	0.07	0.11	0.13	0.16	0.09	0.17	0.00	0.01	0.28	0.14	0.15
CaO	12.21	12.34	12.33	12.13	12.23	11.79	11.43	11.99	12.25	10.69	7.88	2.06	10.95	11.98
Na_2O	1.46	1.37	1.46	1.55	1.84	1.90	2.35	2.15	1.53	5.44	6.92	0.03	1.00	1.27
K_2O	0.10	0.08	0.10	0.11	0.13	0.12	0.16	0.08	0.04	0.02	0.01	0.00	0.03	0.02
F	0.03	0.03	0.00	0.03	0.00	0.00	0.00	0.00	0.04	0.06	0.05	0.01	0.00	0.00
Cl	0.20	0.24	0.26	0.27	0.32	0.10	0.29	0.27	0.25	0.00	0.05	0.01	0.11	0.24
Total	98.46	98.69	99.06	98.12	99.18	99.65	99.07	98.67	98.51	99.33	98.89	97.95	98.32	96.92
Cat/23 Ox														
SiO_2	7.07	7.13	7.01	6.88	6.68	6.66	6.32	6.61	7.05	7.08	7.55	7.50	7.22	7.30
Al_2O_3	1.24	1.16	1.29	1.39	1.71	1.87	2.20	1.70	1.13	4.40	3.73	0.30	1.08	0.85
TiO_2	0.07	0.07	0.08	0.15	0.16	0.15	0.15	0.11	0.12	0.00	0.00	0.02	0.07	0.08
Cr_2O_3	0.01	0.02	0.02	0.02	0.01	0.01	0.02	0.00	0.00	0.00	0.00	0.01	0.00	0.00
MgO	3.65	3.65	3.65	3.47	3.48	2.92	2.74	2.78	3.06	0.00	0.18	5.09	3.38	3.35
FeO	1.05	1.03	1.05	1.17	1.06	1.50	1.75	1.94	1.67	0.03	0.10	2.05	1.55	1.47
MnO	0.01	0.01	0.01	0.01	0.01	0.02	0.02	0.01	0.02	0.00	0.00	0.03	0.02	0.02
CaO	1.85	1.86	1.86	1.86	1.85	1.80	1.79	1.89	1.90	1.49	1.10	0.31	1.68	1.87
Na_2O	0.40	0.37	0.40	0.43	0.50	0.53	0.66	0.61	0.43	1.38	1.75	0.01	0.28	0.36
K_2O	0.02	0.01	0.02	0.02	0.02	0.02	0.03	0.02	0.01	0.00	0.00	0.00	0.00	0.00
F	0.02	0.02	0.00	0.02	0.00	0.00	0.00	0.00	0.02	0.02	0.02	0.00	0.00	0.00
Cl	0.05	0.06	0.06	0.07	0.08	0.02	0.07	0.07	0.06	0.00	0.01	0.00	0.03	0.06
Total	15.44	15.40	15.46	15.49	15.56	15.51	15.76	15.74	15.48	14.41	14.46	15.33	15.31	15.37

	Plagioclase Sample 3645-1130 Analysis Number							Plagioclase Sample 3649-1257 Analysis Number						
	1130PA3	1130PA5	1130PA8	1130PB4	1130PB7	1130PC11	1130PC8	1257PA3	1257PA18	1257PB2	1257PB12	1257PD8	1257PD11	1257PC10
SiO_2	49.61	48.81	48.25	53.93	47.98	48.64	47.34	54.26	54.13	54.82	53.94	58.66	55.68	54.34
Al_2O_3	32.78	32.58	32.52	29.63	32.75	31.73	34.03	28.69	29.13	28.66	29.18	24.99	28.01	28.86
Fe_2O_3	0.20	0.08	0.17	0.18	1.00	0.14	0.10	0.43	0.16	0.12	0.19	1.22	0.19	0.06
CaO	12.51	13.90	14.26	10.42	14.19	13.60	15.22	9.93	10.70	9.96	10.19	5.84	8.90	10.36
Na_2O	3.77	3.31	2.64	5.47	2.93	3.32	2.33	5.71	5.51	6.01	5.68	7.95	6.44	5.73
K_2O	0.01	0.02	0.01	0.00	0.01	0.01	0.00	0.02	0.01	0.00	0.11	0.02	0.00	0.03
Total	98.89	98.69	97.84	99.64	98.86	97.45	99.03	99.05	99.63	99.57	99.28	98.68	99.22	99.38
Cations														
Si	2.27	2.25	2.24	2.44	2.22	2.27	2.18	2.47	2.45	2.48	2.45	2.65	2.52	2.46
Al	1.77	1.77	1.78	1.58	1.78	1.75	1.85	1.54	1.55	1.53	1.56	1.33	1.49	1.54

Table 4. (continued)

	Plagioclase Sample 3645-1130 Analysis Number							Plagioclase Sample 3649-1257 Analysis Number						
	1130PA3	1130PA5	1130PA8	1130PB4	1130PB7	1130PC11	1130PC8	1257PA3	1257PA18	1257PB2	1257PB12	1257PD8	1257PD11	1257PC10
Fe	0.01	0.00	0.01	0.01	0.03	0.00	0.00	0.01	0.01	0.00	0.01	0.04	0.01	0.00
Ca	0.61	0.69	0.71	0.51	0.70	0.68	0.75	0.48	0.52	0.48	0.50	0.28	0.43	0.50
Na	0.34	0.30	0.24	0.48	0.26	0.30	0.21	0.50	0.48	0.53	0.50	0.70	0.56	0.50
K	0.00	0.00	0.00	0.00	0.00	0.00	0.00	0.00	0.00	0.00	0.01	0.00	0.00	0.00
Total	5.00	5.01	4.98	5.01	5.00	5.00	5.00	5.01	5.01	5.02	5.02	5.01	5.01	5.02
norm An	0.65	0.70	0.75	0.51	0.73	0.69	0.78	0.49	0.52	0.48	0.49	0.29	0.43	0.50

[a] Compositions are in wt%.

zircon and monazite. Type III amphiboles may form by alteration of Type II amphiboles to tremolite and chlorite, or by metasomatic introduction of silica and calcium to serpentinized peridotite by hydrothermal fluids (Figure 14). Porphyroclasts of both Type II amphiboles and serpentinite within mats of Type III amphibole suggest that both of these mechanisms were operative.

6.2.2. Interpretation of Peridotite Mineral Chemistry

[48] The mineral chemistry of amphibole in peridotite along with metamorphic mineral associations permits rough estimates of deformation temperatures. Type I amphibole forms by hydration of clinopyroxene during amphibolite-grade crystal-plastic deformation of olivine. Because olivine is stable (not altered to serpentine) temperatures were likely in excess of 500°C [*O'Hanley*, 1996]. The stability of Type I amphibole with orthopyroxene suggests temperatures in excess of 700°C [*Spear*, 1981]. The stability of olivine with type II amphibole suggests a temperature of at least 500°C. Type III tremolitic amphiboles occur with chlorite and/or talc, and contain porphyroclasts of Type II amphibole and serpentinite (Figure 14). Chlorite is stable to temperatures in excess of 700°C in aluminous peridotite [*Frost*, 1975], and thus does not provide a useful temperature constraint. As discussed above, serpentinite porphyroclasts are formed of oxidized chrysotile and lizardite, and contain serpentine vein textures cut by shear zones containing tremolite. There are no textures present to indicate prograde alteration of chrysotile to antigorite, nor has antigorite been observed in any samples, suggesting temperature less than 400°C [*O'Hanley*, 1996]. The fact that the veining texture of serpentinite is cut by type III amphibole indicates that its formation postdated serpentinization. The mineral associations indicating lower temperature formation of type II amphibole relative to type III amphibole is consistent with the lower aluminum and sodium content of type II amphibole [*Spear*, 1981; B. R. Frost, personal communication, 2002]. Type II and type III amphiboles both formed during metasomatic alteration of peridotite by gabbroic magma or hydrothermal fluids. High temperatures (<500°C) permitted aluminum and sodium to be incorporated into the structure of type II amphibole, whereas low temperature during formation of type II amphibole caused aluminum to instead form accompanying chlorite. Overprinting of type II amphibole by type III amphibole

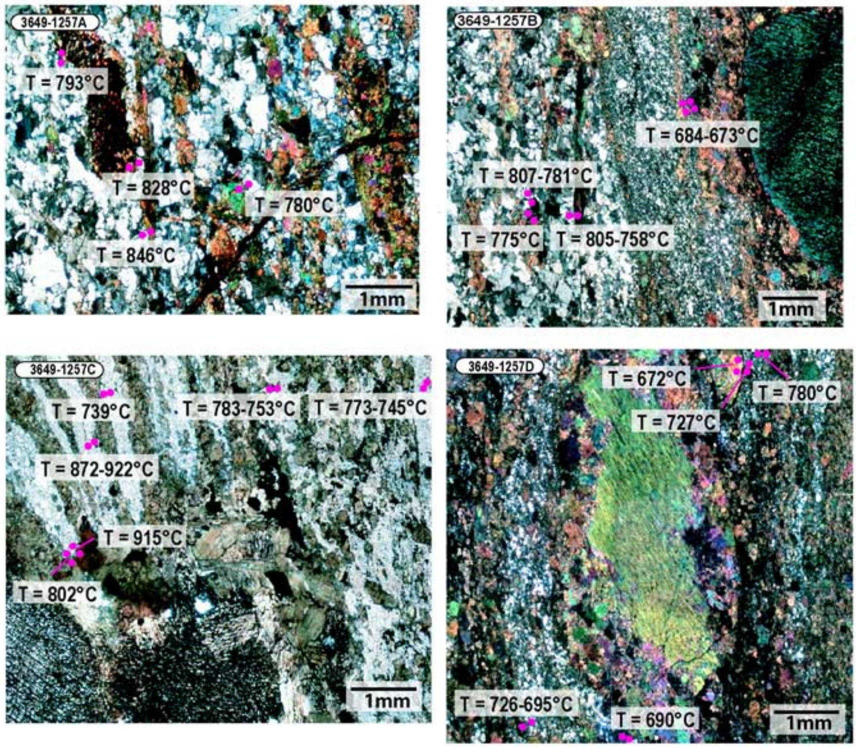

Figure 12. Photomicrographs showing amphibole-plagioclase temperature estimates in sample 3649-1257. Each photomicrograph shows a different area of the sample analyzed for thermometry. Red dots correspond to locations of plagioclase-amphibole pairs analyzed. Note that in area B, temperatures from finely recrystallized plagioclase portion of shear zone are approximately 100°C lower than those from coarsely recrystallized plagioclase, consistent with higher stress deformation at decreasing temperature. Also note that highest calculated temperature (915°C) was calculated from analyses of brown amphibole rimming pyroxene in area C.

during progressive deformation is consistent with denudation by normal faulting.

7. Discussion: Strain Localization on an Oceanic Detachment Fault

[49] Atlantis Massif samples display textures indicating down-temperature deformation from granulite to subgreenschist grade with lower-temperature fabrics and minerals consistently cutting high-temperature fabrics and minerals. This is consistent with tectonic denudation by normal faulting. Ductile deformation fabrics occur over a wide zone (>500 m), whereas semibrittle fabrics are localized in a zone less than 90 m beneath the domal surface. Wholly brittle deformation is localized into a zone less than 10 m below the domal surface. These data along with geomorphic and large-scale geologic characteristics of Atlantis Massif corroborate the oceanic core complex hypothesis. The upper surface of Atlantis Massif is a low-angle normal fault that dips gently ($\leq 20°$) toward the ridge axis along which peridotite and gabbro in the footwall were denuded from deep structural levels. Ductile, high-temperature strain beneath the ridge axis was distributed over a wide region, and strain was localized into progressively narrower zones as the footwall was denuded to shallower structural levels (Figure 15).

7.1. Ductile Strain Localization

[50] Localized granulite- and amphibolite-grade ductile deformation occurs dominantly where gabbro was infused by highly evolved, oxide-rich magmatic fractions. Similar relations of ductile strain partitioning into highly evolved Fe-Ti oxide-rich gabbro and away from lesser-evolved gabbros has been observed at inside corner highs by researchers at Atlantis Bank [*Dick et al.*, 1991; *Cannat*, 1991; *Bloomer et al.*, 1991], and the MARK area [*Agar and Lloyd*, 1997]. These researchers concluded that fractionated oxide-rich magmatic fluids infused solid-state shear zones and provided a rheologic contrast via elevated temperature and/or the presence of a fluid phase to localize strain [*Bloomer et al.*, 1991]. It is also

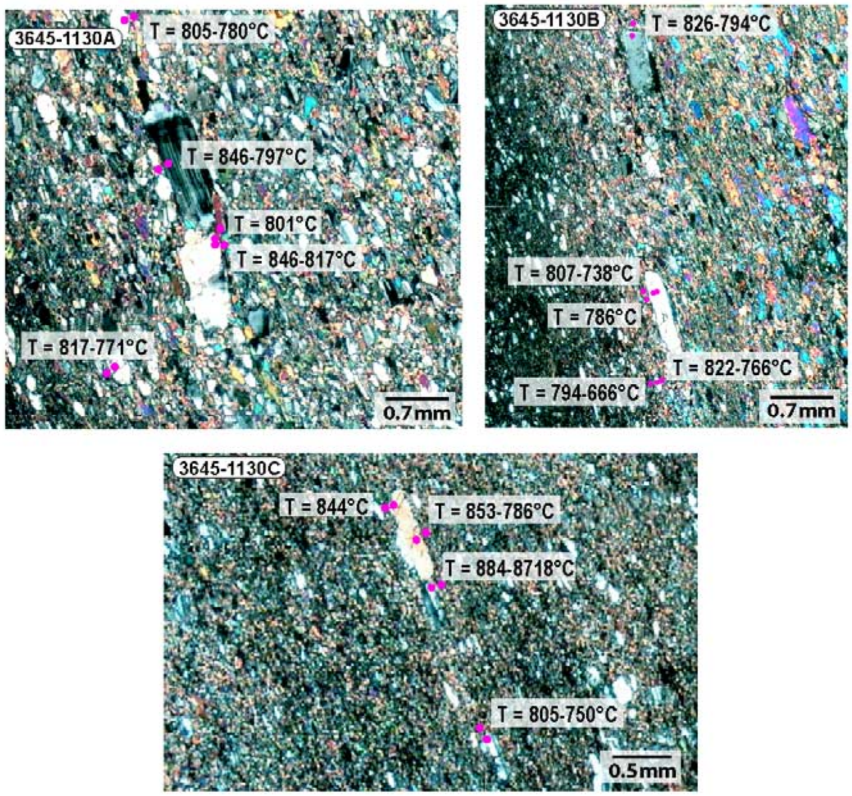

Figure 13. Photomicrographs showing amphibole-plagioclase temperature estimates in sample 3645-1130. Each photomicrograph is of a different area of the sample analyzed for thermometry. Red dots correspond to locations of plagioclase-amphibole pairs analyzed.

possible that solid-state strain is localized into oxide-rich horizons because of the lower strength of oxides compared to silicates [*Agar and Lloyd*, 1997; *Hennig-Michaeli and Seimes*, 1982]. Coarse grained ductile shear zones formed in excess of 750°C are overprinted by finer grained ductile shear zones formed at temperatures less than 750°C.

[51] In peridotite, ductile strain appears to have been localized into zones of metasomatic reaction between primary olivine and pyroxene and oxide-rich magma or hydrothermal fluids that resulted in formation of schistose ''blackwall'' type mineral assemblages that include pargasitic ''type II'' amphibole. Little or no plagioclase was crystallized during these reactions. Apatite was deformed in these shear zones by intracrystalline plasticity, suggesting that apatite crystallized prior to cessation of penetrative deformation. Fe-Ti oxides contain undeformed ilmenite exsolution lamellae in magnetite in both deformed metaperidotite and gabbro samples, suggesting that penetrative, ductile deformation did not occur below temperature of ulvospinel exsolution from titanomagnetite as ilmenite, >650°C (Schroeder, unpublished data). *Cannat and Casey* [1995] noted similar strain localization into zircon and/or ilmenite-rich gabbroic veins in peridotite samples from 15°N on the Mid-Atlantic Ridge. These authors suggest that strain was localized into solidified gabbro and clinopyroxenite veins in peridotite due to thermal contrasts. There is no evidence at Atlantis Massif that clinopyroxene crystallized from gabbroic magma in ductile shear zones, and it is likely that ductile deformation here occurred during metasomatic reactions and the formation of pargasitic amphibole.

7.2. Semibrittle Strain Localization

[52] As footwall rocks were denuded to shallower structural levels and temperature dropped to greenschist-grade conditions (<500°C), strain was partitioned into tremolite-chlorite schist shear zones in peridotite and away from gabbro, unaltered peridotite and serpentinite. Tremolite-chlorite schist is composed of extremely fine-grained mats of intercalated type III amphibole and chlorite that contain undeformed porphyroclasts of type II

Table 5. Representative Compositions of Amphibole Analyzed in Metaperidotite Samples

	Type I Amphibole Samples					Type II Amphibole Samples					Type III Amphibole Samples				
	3646-1205	3646-1205	3646-1205	3646-1205	3646-1205	3652-0950	3652-0950	3652-0950	3652-0950	3652-1309	3652-1309	3652-1309	3652-0950	3652-0950	3652-0950
Wt% analysis															
SiO_2	52.32	57.77	53.81	52.82	52.77	45.76	45.26	45.28	46.41	52.74	49.18	54.68	54.50	56.32	54.72
Al_2O_3	4.64	1.55	2.72	3.16	4.29	11.33	11.37	11.57	10.83	5.14	0.31	0.20	0.69	0.68	0.59
TiO_2	0.13	0.07	0.14	0.21	0.08	1.00	0.97	1.06	0.94	0.12	0.02	0.00	0.00	0.03	0.01
Cr_2O_3	0.93	0.58	0.62	1.06	0.98	1.02	1.23	1.26	1.09	0.16	0.00	0.02	0.07	0.05	0.11
MgO	19.97	23.35	19.02	19.26	19.27	18.08	17.69	18.03	18.65	21.39	18.55	20.86	21.50	24.34	22.43
FeO	7.76	7.10	9.71	8.20	9.24	5.44	5.56	5.32	4.96	3.57	5.38	5.20	4.60	5.86	5.01
MnO	0.20	0.17	0.47	0.30	0.36	0.06	0.07	0.07	0.05	0.05	0.07	0.05	0.11	0.10	0.09
CaO	10.19	6.32	10.57	11.34	10.39	11.94	12.07	12.11	11.91	12.58	10.56	12.37	10.19	8.61	10.20
Na_2O	0.83	0.22	0.52	0.65	0.52	2.74	2.78	3.07	2.70	1.08	0.06	0.06	0.30	0.31	0.24
K_2O	0.04	0.00	0.03	0.05	0.02	0.06	0.08	0.05	0.05	0.02	0.03	0.01	0.02	0.01	0.02
F	0.07	0.00	0.03	0.00	0.03	0.04	0.00	0.00	0.06	0.25	0.00	0.00	0.01	0.00	0.01
Cl	0.02	0.01	0.03	0.03	0.00	0.22	0.20	0.19	0.18	0.04	0.16	0.09	0.13	0.10	0.09
Total	97.07	97.14	97.67	97.06	97.91	97.62	97.25	97.96	97.77	97.03	84.27	93.50	92.08	96.38	93.47
Cation content per 23 oxygen															
Si	7.40	7.96	7.63	7.52	7.45	6.50	6.48	6.44	6.57	7.34	7.92	7.93	7.95	7.86	7.88
Al	0.77	0.25	0.45	0.53	0.71	1.90	1.92	1.94	1.81	0.84	0.06	0.03	0.12	0.11	0.10
Ti	0.01	0.01	0.02	0.02	0.01	0.11	0.10	0.11	0.10	0.01	0.00	0.00	0.00	0.00	0.00
Cr	0.10	0.06	0.07	0.12	0.11	0.12	0.14	0.14	0.12	0.02	0.00	0.00	0.01	0.01	0.01
Mg	4.21	4.79	4.02	4.09	4.06	3.83	3.78	3.82	3.93	4.44	4.45	4.51	4.67	5.06	4.82
Fe	0.92	0.82	1.15	0.98	1.09	0.65	0.67	0.63	0.59	0.42	0.72	0.63	0.56	0.68	0.60
Mn	0.02	0.02	0.06	0.04	0.04	0.01	0.01	0.01	0.01	0.01	0.01	0.01	0.01	0.01	0.01
Ca	1.54	0.93	1.61	1.73	1.57	1.82	1.85	1.84	1.81	1.88	1.82	1.92	1.59	1.29	1.57
Na	0.23	0.06	0.14	0.18	0.14	0.76	0.77	0.85	0.74	0.29	0.02	0.02	0.09	0.08	0.07
K	0.01	0.00	0.01	0.01	0.00	0.01	0.02	0.01	0.01	0.00	0.01	0.00	0.00	0.00	0.00
F	0.03	0.00	0.01	0.00	0.01	0.02	0.00	0.00	0.03	0.11	0.00	0.00	0.00	0.00	0.00
Cl	0.00	0.00	0.01	0.01	0.00	0.05	0.05	0.05	0.04	0.01	0.04	0.02	0.03	0.02	0.02
Al(IV)	0.60	0.04	0.37	0.48	0.55	1.50	1.52	1.56	1.43	0.66	0.06	0.03	0.05	0.11	0.10
AL(VI)	0.18	0.21	0.08	0.05	0.16	0.40	0.40	0.38	0.37	0.18	0.00	0.00	0.07	0.00	0.00
Fe/(Fe + Mg)	0.18	0.15	0.22	0.19	0.21	0.14	0.15	0.14	0.13	0.09	0.14	0.12	0.11	0.12	0.11
100*Na/(Na + Ca)	12.82	5.95	8.16	9.44	8.25	29.34	29.45	31.47	29.11	13.41	0.94	0.90	5.12	6.03	4.11
100*Al/Al + Si	9.46	3.07	5.63	6.59	8.74	22.59	22.85	23.15	21.58	10.30	0.75	0.43	1.47	1.40	1.26
Na + K	0.23	0.06	0.15	0.19	0.14	0.77	0.79	0.86	0.75	0.29	0.02	0.02	0.09	0.08	0.07

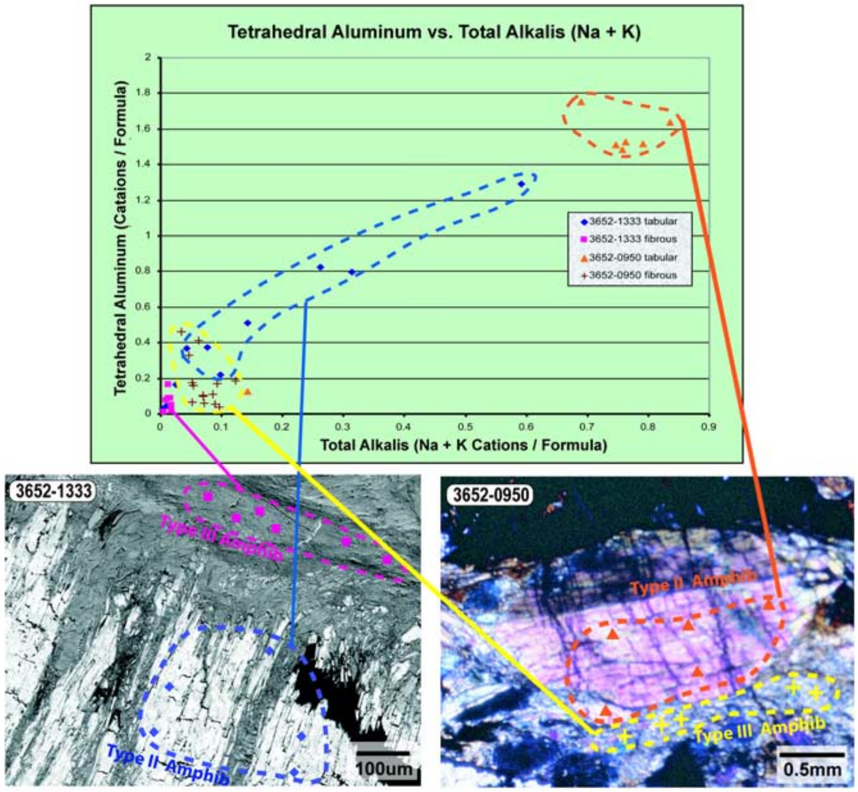

Figure 14. Photomicrographs showing textural variations between type II and type III amphiboles and associated compositions. Early formed (type II) bladed/tabular amphiboles are rich in Al and Na. During late, semibrittle deformation, type II amphiboles are fractured and partially to completely replaced by fine-grained, low Al, Na amphibole (type III).

amphibole and serpentinite. Similar mineral associations are found in blackwall horizons between ophiolitic peridotite bodies and silica- and aluminum-rich continental rocks. The presence of blackwall mineral assemblages along the Atlantis Massif detachment fault indicate that highly reactive fluids infiltrated peridotite along fractures and localized strain via reaction softening. Deformation was accomplished by replacement of ol + cpx + opx by extremely fine-grained aggregates of secondary minerals prone to intergranular slip, and dissolution and precipitation between high-stress and low-stress sites. Continued cataclasis in shear zones could have acted as a positive feed back with diffusive mass transfer by enhancing dissolution of both primary and secondary phases. *Ngwenya et al.* [2000] experimentally determined that quartz activity in pore fluids increased by three orders of magnitude during cataclasis. Similarly, in compaction creep experiments on calcite aggregates, *Zhang et al.* [2002] found that strain rate was dramatically higher in the presence of a reactive pore fluid as opposed to a nonreactive pore fluid.

[53] Textures of tremolite-chlorite schists are very similar to paracrystalline microboudinage noted by *Misch* [1969, 1970] in studies of ultramafic amphibolites in the Cascades, and ophiolitic shear zones in the North Cascades studied by *Miller* [1988]. He proposed that strain in the ultramafic Ingalls Complex was localized by fluid flow and metasomatism of peridotite to tremolitic amphibole and chlorite. Though deformation likely occurred in very different tectonic settings, similar processes of fluid flow and metasomatic reaction appears to have been responsible for strain localization on the Atlantis Massif detachment fault. Similar mechanism have been suggested for localizing strain and significantly reducing crustal strength in quartzofeldspathic continental rocks [*Wintsch and Yi*, 2002].

[54] The veining structures of undeformed serpentinite porphyroclasts are cut by the foliation in semibrittle tremolite-chlorite schist shear zones. These relations indicate that peridotite was at least locally serpentinized between ductile and semibrittle deformation. The relative timing of the bulk

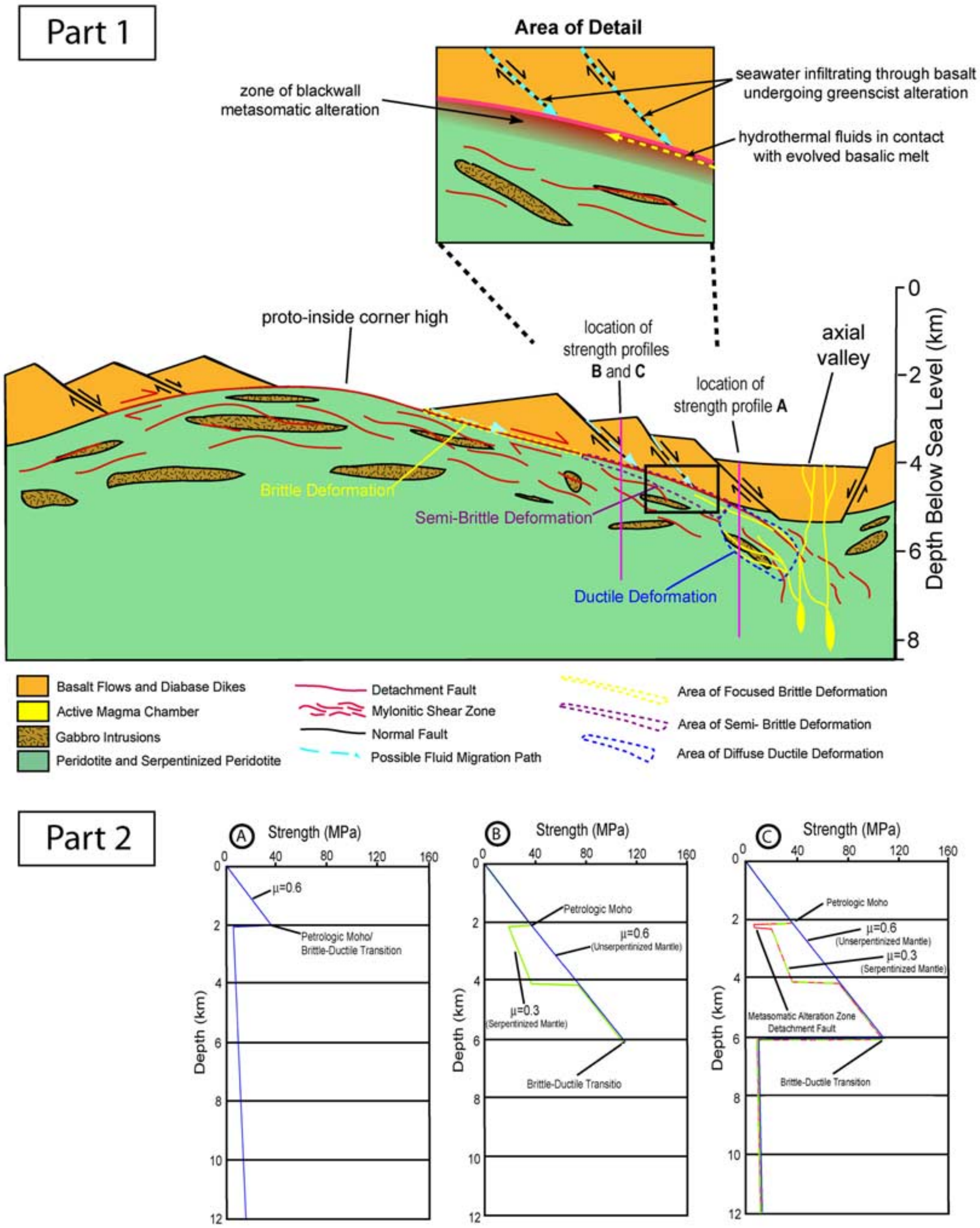

Figure 15. Schematic cross section of Atlantis Massif with hypothetical strength curves. Part 1: Schematic cross section (no vertical exaggeration) showing possible fault orientation and zones of deformation during active low-angle normal faulting at Atlantis Massif. Diffuse high-temperature beneath the ridge axis occurs concurrently with localized low-temperature at shallow levels of the fault. Area of detail shows zone of metasomatic blackwall alteration and possible sources of fluids responsible for alteration. Part 2: Hypothetical strength profiles for several locations and conditions during faulting; all three profiles assume that the petrologic Moho is at 2 km below the seafloor. Profile A is a near-axis profile of possible strength conditions assuming the brittle-ductile transition is located at the petrologic Moho. Profile B shows possible off-axis strength in which cooling has lowered the brittle-ductile transition to a depth of 6 km, and serpentinization has reduced the strength of the upper 2 km of the mantle. Profile C illustrates hypothesized strength profile at Atlantis Massif, in which metasomatic alteration and reaction softening within a narrow zone lowered strength below that of normal serpentinite and allowed for localized deformation on the detachment fault.

of serpentinization and the localization of shear strain on the detachment fault is not known, but some serpentinization must have preceded semi-brittle strain to produce serpentinite porphyroclasts. Oxygen isotopic ratios in epidote and quartz from the Whipple Mountain core complex (Colorado River extensional corridor, SE California) indicate that cataclasite from the detachment fault zone was approximately 80°C cooler than rock 50 m structurally beneath the detachment during peak deformation [*Morrison and Anderson*, 1998]. These authors propose this temperature discrepancy was caused by refrigeration of the fault zone by circulation of surface fluids. It is possible that fluid circulation at Atlantis Massif caused similar cooling, leading to serpentinization and greenschist-grade metasomatism within the narrow fault zone, while rock at structurally deeper levels remained at amphibolite-grade temperatures. This process could cause the bulk of serpentinization to occur following semibrittle and brittle deformation, explaining the static serpentinization textures.

7.3. Brittle Strain Localization

[55] Strong brittle deformation fabrics in most instances directly overprint semibrittle tremolite-chlorite schist shear zones. Only weak brittle deformation fabrics are observed overprinting serpentinization textures or crystal-plastic shear zones. This suggests that fluids and/or reaction-weakening processes responsible for localizing semibrittle strain also influence brittle strain localization.

8. Implications

8.1. Rheology of Peridotite-Dominated Oceanic Lithosphere

[56] Deformation texture relations at Atlantis Massif demonstrate that rheology and strain localization in peridotite-dominated oceanic lithosphere can be controlled by varying factors during extensional faulting. Deformation mechanisms at Atlantis Massif are a function of temperature, structural depth, and the availability and reactivity of pore fluids. Fault slip occurred via multiple deformation mechanisms active simultaneously at differing structural levels.

[57] Early formed textures indicate viscous deformation by both crystal plasticity and diffusive mass transfer at high-temperature (>500°C). Activity of both of these mechanisms over the same temperature range in gabbro and peridotite indicates that the presence of reactive fluids controlled accommodation of viscous strain. Transfer of viscous strain between multiple interlayered lithologies and two possible deformation mechanisms should be considered when modeling faulting at slow-spreading mid-ocean ridges.

[58] Localization of low-temperature (<500°C) semibrittle shear strain into zones of "blackwall" type altered peridotite and away from serpentinized peridotite suggests that reaction softening may have weakened peridotite more than serpentinization. Serpentinization of peridotite (during which the coefficient of friction lowered from ~0.6 to ~0.3) [*Escartín et al.*, 1997a, 1997b, 2001] has been suggested as mechanisms to reduce strength and permit long-lived slip on low-angle normal faults in oceanic lithosphere. Rotary shear experiments on halite/kaolinite aggregates with reactive brine pore fluids performed by *Bos and Spires* [2001] show that the solution transfer and associated grain boundary sliding at low temperatures (<300°C) can causes a transition from frictional behavior governed by Byerlee's law to viscous/ductile flow that is independent of normal stress. While these experiments were performed on clays and have been suggested to apply to mica-rich continental rocks, experimentally produced microstructures are visually very similar to those of Atlantis Massif tremolite/chlorite schists. It is possible that high rates of solution transfer during alteration of peridotite combined with sliding along extremely fine grains caused viscous flow along the Atlantis Massif detachment fault. At present, it is impossible to determine the viscosity of this shear zone because no strength experiments have been performed on rocks of this composition under such conditions.

[59] Figure 15 (Part II) shows hypothetical schematic crustal strength profiles for several locations and situations during evolution of the Atlantis Massif detachment fault system. All three profiles assume lithosphere consisting of basalt above and peridotite below a basal detachment at 2 km depth. Profile A illustrates that viscous/ductile deformation may be distributed over a wide zone beneath a shallow brittle/ductile transition in the neovolcanic zone at the ridge axis. Profiles B and C show possible off-axis profiles assuming brittle/frictional behavior governed by Byerlee's law from 0 km to 6 km (assuming a geothermal gradient of 100°C per kilometer depth on the ridge flank and a brittle ductile transition at 600°C in peridotite) depth and viscous behavior below 8 km depth. Profile B assumes basalt with a friction coefficient of 0.6

from 0 km to 2 km depth, serpentinized peridotite with a friction coefficient of 0.3 from 2 km to 4 km depth, and unaltered peridotite with a friction coefficient from 4 km to 8 km depth. Under these conditions, the lithosphere would contain a wide zone of rock with significantly reduced frictional strength. Profile C shows the hypothesized strength curve during detachment faulting at Atlantis Massif. In this curve, there is also a wide zone of serpentinized peridotite with reduced frictional strength, but a narrow zone at 2 km depth allows viscous flow along the detachment fault via solution-enhanced cataclasis and intense alteration of peridotite.

8.2. Low-Angle Normal Faults Tectonics

[60] Deformation texture studies of several oceanic core complexes reveal that strain may be localized onto detachment faults over a wide range of temperature. Deformed gabbros at Atlantis Bank [*Cannat*, 1991; *Miranda et al.*, 2002], and the MARK area [*Agar and Lloyd*, 1997, *Cannat et al.*, 1997] indicate strain localization at amphibolite grade followed by low-temperature deformation. A study of a core complex at 15°N on the Mid-Atlantic Ridge indicates strain localization in peridotite at greenschist- and subgreenschist-grade conditions and no high-temperature deformation [*MacLeod et al.*, 2002; *Escartín et al.*, 2003]. Deformation textures at Atlantis Massif indicate that strain is initially localized into gabbro and peridotite at granulite and amphibolite grade over a wide zone, then into a narrow (100 m wide) fault in metaperidotite at greenschist and subgreenschist grade. In spite of these differences in lithology and strain localization, the resulting core complex dome and detachment fault geometry are nearly identical at all four sites. Additionally, core complex morphology and fault geometry are nearly identical between oceanic and continental detachment fault systems, which form in completely different tectonic settings and lithosphere with different strength characteristics. These data suggest that initiation of low-angle normal faults and formation of metamorphic core complexes may be independent of temperature, rock strength and mechanisms of strain localization. It is possible that low-angle normal faults develop in situations where the stress field is aligned such that the maximum and minimum principle stresses are oriented inclined to the vertical and horizontal axes as suggested by *Parsons and Thompson* [1993] and *Campbell-Stone et al.* [2000]. Orientation and offset direction of conjugate shear fractures in sample 3652-0937 (Figure 9) suggest that this may have been the case within the Atlantis Massif detachment fault. Extensional deformation during which processes such as magma injection or basal traction cause rotation of principle stresses away from vertical and horizontal axes may lead to the formation of low-angle normal faults and metamorphic core complexes in a variety of tectonic settings and rock types.

9. Conclusions

[61] The following conclusions can be drawn from this textural and mineral chemistry study of Atlantis Massif:

[62] 1. The upper surface of Atlantis Massif is an exposed detachment (normal) fault dipping beneath the Mid-Atlantic Ridge axis upon which peridotite with gabbro intrusions were tectonically denuded to form the central dome of the massif.

[63] 2. Early ductile strain was penetrative over a broad range of structural depth (>500 m) beneath the ridge axis. In peridotite, ductile strain was localized into discrete shear zones containing aluminous amphibole and incompatible-rich accessory minerals by infusion of gabbroic melt or hydrothermal fluids at temperatures in excess of 600°C. Strain was accommodated in these zones by a combination of crystal plastic flow and diffusive mass transfer. In gabbro, ductile strain was accommodated by crystal plastic flow of plagioclase in mylonitic shear zones, and by diffusive mass transfer with grain boundary sliding in hornblende schists.

[64] 3. Semibrittle strain is localized into a zone <100 m beneath the main detachment surface and brittle strain is localized less than 10 m beneath the detachment. Semibrittle strain is accommodated by a combination of cataclasis and diffusive mass transfer in schistose shear zones containing peridotite altered to blackwall mineral assemblages including tremolite, chlorite, and sometimes aragonite and talc. Strain was localized by reaction softening during which cataclasis in the presence of highly reactive pore fluids may have caused a transition from frictional slip to viscous flow along the fault.

Appendix A: Analytical and Data Processing Methods

A1. Analytical Technique

[65] Mineral compositions were analyzed on polished, carbon-coated thin sections with a JEOL

JXA-8900 five-spectrometer electron microprobe. Measurements were made with a focused beam, using a beam current of 20 nA and accelerating voltage of 15 kV. For amphibole and chlorite analyses Si, Al, Ti, Mg, Fe, Ca, Na, K, Mn and Cr were counted for 20 seconds s each, and F and Cl were counted for 10 seconds s. For plagioclase analyses Fe and K were counted for 20 seconds s each and Si, Al, Ca and Na were counted for 10 seconds each. Spectral data was corrected with a standard ZAF correction.

A2. Gabbro Mineral Chemistry and Plagioclase-Hornblende Thermometry

[66] Deformation temperature estimates were made using the modified hornblende-plagioclase geothermometer [*Holland and Blundy*, 1994]. This method uses the ΔG of two possible equilibria to estimate temperature at varying pressures. Equilibrium B described by *Holland and Blundy* [1994] is based on the exchange of aluminum and sodium between amphibole and plagioclase by the reaction:

$$\text{edenite} + \text{albite} = \text{richterite} + \text{anorthite}$$

This equilibrium does not require quartz saturation and can therefore be applied to a wide range of rocks. Equilibrium A described by *Holland and Blundy* [1994] was not used to estimate temperatures as it requires quartz saturation, and free quartz has not been observed in the gabbro samples investigated.

[67] Amphibole compositions were measured in pairs at distances from the grain boundaries ranging from 20 μm to 50 μm in samples 3649-1257 and 3645-1130. Composition from pairs distal to the grain boundaries yielded more consistent and stable temperatures than proximal pairs. Representative amphibole and plagioclase compositions are presented in Table 3. Partitioning of total iron between FeO and Fe_2O_3 was done by the method described by *Dale et al.* [2000]. A pressure of 1.5 kbar was assumed for temperature calculations as gabbro was likely emplaced less then 5 km below the surface. Varying the input pressure from 0–5 kb in trial calculations changed the calculated temperature by less than 5°C total. Temperature estimates range between 915°C and 650°C. Analyzed data points and calculated temperatures are shown in Figures 12 and 13.

[68] Possible sources of error in temperature estimates include: analytical uncertainty, low-temperature ion exchange across grain boundaries, nonequilibrium between plagioclase and amphibole, and uncertainty of the thermometer. The wide range in deformation temperature of sample 3649-1257 (915°C to 673°C) is at least partially due to a protracted deformation history that occurred during cooling through this temperature range. Deformation textures and minerals in sample 3649-1257 indicate that deformation occurred over the transition from granulite to middle-amphibolite facies, so a wide range of temperatures should be expected. The deformation temperature range in sample 3645-1130 (850°C–656°C) may be due to analytical errors, thermometer uncertainty or nonequilibrium between amphibole matrix and plagioclase porphyroclasts.

Acknowledgments

[69] We acknowledge the captain and crew of the R/V *Atlantis* and Woods Hole Oceanographic Institution Deep Sea Operations Group; chief scientist of the MARVEL 2000 Cruise Donna Blackman; B. Ron Frost, Greg Hirth, Susan Swapp and Jan Tullis for insight and/or reviews of metamorphic and deformation history or Atlantis Massif. Funding for this work was provided by a subcontract to John from the National Science Foundation through Scripps Institute of Oceanography.

References

Agar, S. M., and G. E. Lloyd (1997), Deformation of Fe-Ti oxides in gabbroic shear zones from the MARK area, *Proc. Ocean Drill. Program Sci. Results*, *156*, 123–141.

Bestmann, M., K. Kunze, and A. Matthews (2000), Evolution of a calcite marble shear zone complex on Thassos Island, Greece: Microstructural and textural fabrics and their kinematic significance, *J. Struct. Geol.*, *22*, 1789–1807.

Blackman, D. K., J. R. Cann, B. Janssen, and D. K. Smith (1998), Origin of extensional core complexes: Evidence from the Mid-Atlantic Ridge at Atlantis Fracture Zone, *J. Geophys. Res.*, *103*, 21,315–21,333.

Blackman, D. K., et al. (2004), Geology of the Atlantis Massif (Mid-Atlantic Ridge, 30°N): Implications for the evolution of an ultramafic oceanic core complex, *Mar. Geophys. Res.*, *23*, 443–469.

Bloomer, S. H., P. S. Meyer, H. J. B. Dick, K. Ozawa, and J. H. Natland (1991), Texture and mineralogic variations in gabbroic rocks from Hole 735B, *Proc. Ocean Drill. Program Sci. Results*, *118*, 21–40.

Bos, B., and C. J. Spires (2001), Experimental investigation into the microstructural and mechanical evolution of phyllosilicate-bearing fault rock under conditions favoring pressure solution, *J. Struct. Geol.*, *23*, 1187–1202.

Brodie, K. H., and E. H. Rutter (1985), On the relationship between deformation and metamorphism, with special reference to the behavior of basic rocks, in *Metamorphic Reactions: Kinetics, Textures, and Deformation*, edited by A. B. Thompson and D. C. Rubie, pp. 138–179, Springer-Verlag, New York.

Campbell-Stone, E. A., B. E. John, J. W. Geissman, D. A. Foster, and R. Livicarri (2000), Mechanisms for accommodation of Miocene extension: Low-angle normal faulting, magmatism, and secondary breakaway faulting in the southern Sacramento Mountains, southeastern California, *Tectonics*, *19*, 566–587.

Cann, J. R., D. K. Blackman, D. K. Smith, E. McAllister, B. Janssen, S. Mello, E. Avgerinos, A. R. Pascoe, and J. Escartín (1997), Corrugated slip surfaces formed at North Atlantic ridge-transform intersections, *Nature*, *385*, 329–332.

Cannat, M. (1991), Plastic deformation at an oceanic spreading ridge: A microstructural study of the Site 735 gabbros (Southwest Indian Ocean), *Proc. Ocean Drill. Program Sci. Results*, *118*, 399–406.

Cannat, M., and J. F. Casey (1995), An ultramafic lift at the Mid-Atlantic Ridge: Successive stages of magmatism in serpentinized peridotites from the 15°N region, in *Mantle and Lower Crust Exposed in Oceanic Ridges and in Ophiolites*, edited by R. L. M. Vissers and A. Nicolas, pp. 5–34, Kluwer Acad., Norwell, Mass.

Cannat, M., Y. Lagabrielle, H. Bougault, J. Casey, N. de Coutures, L. Dmitriev, and Y. Fouquet (1997), Ultramafic and gabbroic exposures at the Mid-Atlantic Ridge: Geological mapping in the 15°N region, *Tectonophysics*, *279*, 193–213.

Chery, J. (2001), Core complex mechanics; from the Gulf of Corinth to the Snake Range, *Geology*, *29*, 439–442.

Chidester, A. H. (1962), Petrology and geochemistry of selected talc-bearing ultramafic rocks and adjacent country rocks in north-central Vermont, *U.S. Geol. Surv. Prof. Pap.*, *345*, 207 pp.

Christie, D. M., B. P. West, and D. G. Pyle (1997), Extreme morphologic and petrologic diversity within the Southeast Indian Ridge (abstract), *Eos Trans. AGU*, *78*(46), Fall Meet. Suppl., F673.

Crittenden, M. D., Jr., P. J. Coney, and G. H. Davis (Eds.) (1980), *Cordilleran Metamorphic Core Complexes*, *Mem. Geol. Soc. Am.*, *153*, 490 pp.

Dale, J., T. Holland, and R. Powell (2000), Hornblende-garnet-plagioclase thermobarometry: A natural assemblage calibration of the thermodynamics of hornblende, *Contrib. Mineral. Petrol.*, *140*, 353–362.

Davis, G. A., J. L. Anderson, E. G. Frost, and T. J. Shackelford (1980), Mylonitization and detachment faulting in the Whipple-Buckskin-Rawhide Mountains terrane, southeastern California and western Arizona, in *Cordilleran Metamorphic Core Complexes*, *Mem. Geol. Soc. Am.*, *153*, 79–129.

Davis, G. H., G. S. Lister, and S. R. Reynolds (1986), Structural evolution of the Whipple and South Mountain shear zones, southwestern United States, *Geology*, *14*, 7–10.

Dick, H. J. B., W. B. Bryan, and G. Thompson (1981), Low-angle detachment faulting and steady-state emplacement of plutonic rocks at ridge-transform intersections (abstract), *Eos Trans. AGU*, *62*, 406.

Dick, H. J. B., H. Schouten, P. S. Meyer, D. G. Gallo, H. Bergh, R. Tyce, P. Patriat, K. T. M. Johnson, J. Snow, and A. Fischer (1991), Tectonic evolution of the Atlantis II Fracture Zone, *Proc. Ocean Drill. Program Sci. Results*, *118*, 359–398.

Dick, H. J. B., J. H. Natland, and D. J. Miller (1999), *Proceedings of the Ocean Drilling Program Initial Report*, vol. 176, Ocean Drill. Program, College Station, Tex.

Ehlers, T. A., P. A. Armstrong, and D. S. Chapman (2001), Normal fault thermal regimes and the interpretation of low-temperature thermochronometers, *Phys. Earth Planet. Inter.*, *126*, 179–194.

Escartín, J., and M. Cannat (1999), Ultramafic exposures and the gravity signature of the lithosphere near the Fifteen-Twenty Fracture Zone (Mid-Atlantic Ridge, 14°–16.5°N), *Earth Planet. Sci. Lett.*, *171*, 411–424.

Escartín, J., G. Hirth, and B. Evans (1997a), Non-dilatant brittle deformation of serpentinites: Implications for Mohr-Coulomb theory and the strength of faults, *J. Geophys. Res.*, *102*, 2897–2913.

Escartín, J., G. Hirth, and B. Evans (1997b), Effects of serpentinization on the lithospheric strength and the style of normal faulting at slow-spreading ridges, *Earth Planet. Sci. Lett.*, *151*, 181–190.

Escartín, J., G. Hirth, and B. Evans (2001), Strength of slightly serpentinized peridotites: Implications for the tectonics of oceanic lithosphere, *Geology*, *29*, 1023–1026.

Escartín, J., C. Mével, C. J. MacLeod, and A. M. McCaig (2003), Constraints on deformation conditions and the origin of oceanic detachments: The Mid-Atlantic Ridge core complex at 15°45′N, *Geochem. Geophys. Geosyst.*, *4*(8), 1067, doi:10.1029/2002GC000472.

Fayon, A. K., D. L. Whitney, C. Teyssier, J. I. Garver, and Y. Dilek (2001), Effects of plate convergence obliquity on timing and mechanisms of exhumation of a mid-crustal terrain, the Central Anatolian Crystalline Complex, *Earth Planet. Sci. Lett.*, *192*, 191–205.

Floyd, J. S., J. C. Mutter, A. M. Goodliffe, and B. Taylor (2001), Evidence for fault weakness and fluid flow within an active low-angle normal fault, *Nature*, *411*, 779–783.

Frost, B. R. (1975), Central metamorphism of serpentinite, chloritic blackwall and rodingite at Paddy-Go-Easy Pass, central Cascades, Washington, *J. Petrol.*, *16*, 273–313.

Gessner, K., U. Ring, C. Johnson, R. Hetzel, C. W. Passchier, and T. Gungor (2001), An active bivergent rolling-hinge detachment system: Central Menderes metamorphic core complex in western Turkey, *Geology*, *29*, 611–614.

Hennig-Michaeli, C., and J. Seimes (1982), Compression experiments on natural magnetite crystals at 200°C and 400°C at 400 MPa confining pressure, in *Issues in Rock Mechanics: 23rd Symposium*, edited by R. E. Godman and F. E. Heuze, pp. 380–388, Soc. for Min., Metall. and Explor., Littleton, Colo.

Hirth, G., and J. Tullis (1992), Dislocation creep regimes in quartz aggregates, *J. Struct. Geol.*, *14*, 145–159.

Holland, T., and J. Blundy (1994), Non-ideal interactions in calcic amphiboles and their bearing on amphibole-plagioclase thermometry, *Contrib. Mineral. Petrol.*, *116*, 433–447.

Jaroslow, G. E., H. J. B. Dick, and G. Hirth (1996), Abyssal peridotite mylonites: Implications for grain-size sensitive flow and strain partitioning in the oceanic lithosphere, *Tectonophysics*, *256*, 17–37.

John, B. (1987), Geometry and evolution of a mid-crustal extension fault system: Chemeuevi Mountains, southeastern California, in *Continental Extensional Tectonics*, edited by M. P. Coward, J. F. Dewey, and P. L. Hancock, *Geol. Soc. Spec. Publ.*, *28*, 313–335.

Kelley, D. S., et al. (2001), An off-axis hydrothermal vent field near the Mid-Atlantic Ridge at 30°N, *Nature*, *411*, 145–149.

MacLeod, C. J., J. Escartín, D. Banerji, G. J. Banks, M. Gleeson, D. H. B. Irving, R. M. Lilly, A. M. McCaig, Y. Niu, and D. K. Smith (2002), Direct evidence for oceanic detachment faulting at the Mid-Atlantic Ridge, 15°45′N, *Geology*, *30*(10), 879–882.

Miller, R. B. (1988), Fluids flow, metasomatism and amphibole deformation in an imbricated ophiolite, North Cascades, Washington, *J. Struct. Geol.*, *10*, 283–296.

Miranda, E. A., B. E. John, G. Hirth, and H. Dick (2002), Structural development of an oceanic detachment fault system, Atlantis Bank, Southwest Indian Ridge, *Eos Trans. AGU*, *83*(47), Fall Meet. Suppl., Abstract T11A-1234.

Misch, P. (1969), Paracrystalline microboudinage of zoned grains and other criteria for synkinematic growth of metamorphic minerals, *Am. J. Sci.*, *267*, 43–63.

Misch, P. (1970), Paracrystalline microboudinage in a metamorphic reaction sequence, *Geol. Soc. Am. Bull.*, *81*, 2483–2485.

Mitchell, N. C., J. Escartín, and S. Allerton (1998), Detachment faults at mid-ocean ridges garner interest, *Eos Trans. AGU*, *79*, 127.

Morrison, J., and J. L. Anderson (1998), Footwall refrigeration along a detachment fault: Implications for the thermal evolution of core complexes, *Science*, *279*, 63–66.

Mutter, M. C., and J. A. Karson (1992), Structural processes at slow-spreading ridges, *Science*, *257*, 627–634.

Ngwenya, B. T., S. C. Elphick, I. G. Main, and G. B. Shimmield (2000), Experimental constraints on the diagenetic self healing capacity of faults in high porosity rocks, *Earth Planet. Sci. Lett.*, *183*, 187–199.

O'Hanley, D. S. (1992), Solution to the volume problem in serpentinization, *Geology*, *20*, 705–708.

O'Hanley, D. S. (1996), *Serpentinites*, 277 pp., Oxford Univ. Press, New York.

Parsons, T., and G. A. Thompson (1993), Does magmatism influence low-angle normal faulting?, *Geology*, *21*, 247–250.

Ranero, C., and T. J. Reston (1999), Detachment faulting at ocean core complexes, *Geology*, *27*, 983–986.

Schroeder, T., B. John, and B. R. Frost (2002), Geologic implications of seawater circulation through peridotite exposed at slow-spreading mid-ocean ridge, *Geology*, *30*, 367–370.

Searle, R. C., H. Fujioka, M. Cannat, C. Mevel, H. Fujimoto, and L. M. Parson (1999), FUJI Dome, a large detachment fault near 64 degrees E on the very slow spreading South West Indian Ridge (abstract), *Eos Trans. AGU*, *80*(46), Fall Meet. Suppl., F956.

Spear, F. S. (1981), An experimental study of hornblende stability and compositional variability in amphibolite, *Am. J. Sci.*, *281*, 679–734.

Spencer, J. E. (1984), Role of tectonic denudation in warping and uplift of low-angle normal faults, *Geology*, *12*, 95–98.

Spencer, J. E., and S. J. Reynolds (1989), Middle tertiary tectonics of Arizona and adjacent areas, in *Geologic Evolution of Arizona*, Digest 17, edited by J. P. Jenney and S. J. Reynolds, pp. 539–574, Ariz. Geol. Soc., Tucson.

Tamaki, K., and C. Mevel (1998), Spreading tectonics of the eastern part of the Southwestern Indian Ridge: A synthesis of FUJI expedition (abstract), *Eos Trans. AGU*, *79*(46), Fall Meet. Suppl., F892.

Tucholke, B. E., J. Lin, M. C. Kleinrock, M. Tivey, T. B. Reed, J. Goff, and G. E. Jaroslow (1997), Segmentation and crustal structure of the western Mid-Atlantic Ridge flank, 25°25′–27°10′N and 0–29 m.y., *J. Geophys. Res.*, *102*, 10,203–10,223.

Tucholke, B. E., J. Lin, and M. C. Kleinrock (1998), Megamullions and mullion structure defining oceanic metamorphic core complexes on the Mid-Atlantic Ridge, *J. Geophys. Res.*, *103*, 9857–9866.

Tucholke, B. E., K. Fujioka, T. Ishihara, G. Hirth, and M. Kinoshita (2001), Submersible study of an oceanic megamullion in the central North Atlantic, *J. Geophys. Res.*, *106*, 16,145–16,161.

Tullis, J., and R. A. Yund (1987), Transition from cataclastic flow to dislocation creep of feldspar: Mechanisms and microstructures, *Geology*, *15*, 606–609.

Wernicke, B. (1981), Low-angle normal faults in the Basin and Range province: Nappe tectonics in an extending orogen, *Nature*, *291*, 645–648.

Wintsch, R. P., and K. Yi (2002), Dissolution and replacement creep: A significant deformation mechanism in mid-crustal rocks, *J. Struct. Geol.*, *24*, 1179–1193.

Zhang, J., Y. Zheng, and S. Liu (2000), Application of general shear theory to the study of formation mechanism of the metamorphic core complex: A case study of Xiaoqinling in central China, *Acta Geol. Sin.*, Engl. Transl., *74*, 19–28.

Zhang, X., J. Salemans, C. J. Peach, and C. J. Spires (2002), Compaction experiments on wet calcite powder at room temperature: Evidence for operation of intergranular pressure solution, in *Deformation Mechanisms, Rheology and Tectonics: Current Status and Future Perspectives*, edited by S. Meer et al., *Geol. Soc. Spec. Publ.*, *200*, 29–39.